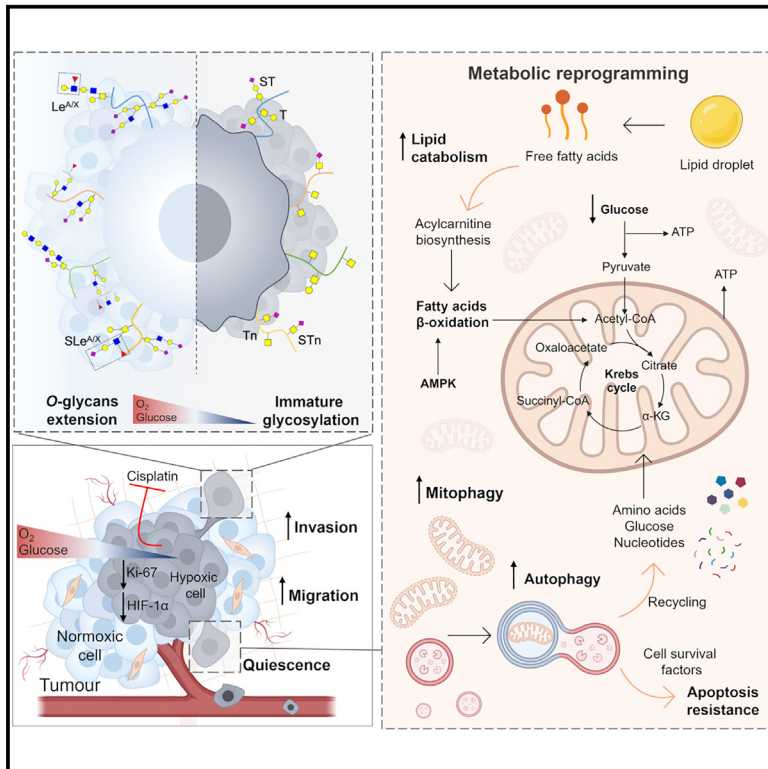


Multilevel plasticity and altered glycosylation drive aggressiveness in hypoxic and glucose-deprived bladder cancer cells

Graphical abstract



Authors

Andreia Peixoto, Dylan Ferreira, Andreia Miranda, ..., André M.N. Silva, Lúcio Lara Santos, José Alexandre Ferreira

Correspondence

jose.a.ferreira@ipopoporto.min-saude.pt

In brief

Health sciences; Medicine; Medical specialty; Internal medicine; Oncology; Natural sciences; Biological sciences; Systems biology; Cancer systems biology; Cancer

Highlights

- BLCA cells resist low oxygen and glucose, stopping proliferation and enhancing invasion
- Stressed cells rely on mitophagy and fatty acid β -oxidation for energy
- BLCA cells and tumors display immature glycophenotypes in response to stress
- Stress-induced immature glycosylation drives resistance to anoikis and invasion



Article

Multilevel plasticity and altered glycosylation drive aggressiveness in hypoxic and glucose-deprived bladder cancer cells

Andreia Peixoto,^{1,2,3} Dylan Ferreira,^{1,2,3,12} Andreia Miranda,^{1,2,3,12} Marta Relvas-Santos,^{1,2,3,4} Rui Freitas,^{1,2,3} Tim S. Veth,^{5,6} Andreia Brandão,¹ Eduardo Ferreira,¹ Paula Paulo,¹ Marta Cardoso,¹ Cristiana Gaitero,^{1,3} Sofia Cotton,^{1,3} Janine Soares,^{1,3,7} Luís Lima,¹ Filipe Teixeira,⁸ Rita Ferreira,⁷ Carlos Palmeira,^{1,9,10} Albert J.R. Heck,^{5,6} Maria José Oliveira,^{2,3} André M.N. Silva,⁴ Lúcio Lara Santos,^{1,10,11} and José Alexandre Ferreira^{1,3,13,*}

¹Research Center of IPO-Porto (CI-IPOP) / CI-IPOP@RISE (Health Research Network), Portuguese Oncology Institute of Porto (IPO-Porto) / Porto Comprehensive Cancer Center (P.ccc) Raquel Seruca, Porto, Portugal

²i3S – Instituto de Investigação e Inovação em Saúde, Universidade do Porto, Porto, Portugal

³School of Medicine and Biomedical Sciences (ICBAS), University of Porto, Porto, Portugal

⁴LAQV-REQUIMTE, Department of Chemistry and Biochemistry, Faculty of Sciences, University of Porto, Porto, Portugal

⁵Biomolecular Mass Spectrometry and Proteomics, Bijvoet Center for Biomolecular Research and Utrecht Institute for Pharmaceutical Sciences, University of Utrecht, Utrecht, the Netherlands

⁶Netherlands Proteomics Center, Padualaan, Utrecht, the Netherlands

⁷QOPNA & LAQV-REQUIMTE, Department of Chemistry, University of Aveiro, Aveiro, Portugal

⁸Centre of Chemistry, University of Minho, Braga, Portugal

⁹Department of Immunology, Portuguese Oncology Institute of Porto, Porto, Portugal

¹⁰Health School of University Fernando Pessoa, Porto, Portugal

¹¹Department of Surgical Oncology, Portuguese Oncology Institute of Porto, Porto, Portugal

¹²These authors contributed equally

¹³Lead contact

*Correspondence: jose.a.ferreira@ipoporito.min-saude.pt

<https://doi.org/10.1016/j.isci.2025.111758>

SUMMARY

Bladder tumors with aggressive characteristics often present microenvironmental niches marked by low oxygen levels (hypoxia) and limited glucose supply due to inadequate vascularization. The molecular mechanisms facilitating cellular adaptation to these stimuli remain largely elusive. Employing a multi-omics approach, we discovered that hypoxic and glucose-deprived cancer cells enter a quiescent state supported by mitophagy, fatty acid β -oxidation, and amino acid catabolism, concurrently enhancing their invasive capabilities. Reoxygenation and glucose restoration efficiently reversed cell quiescence without affecting cellular viability, highlighting significant molecular plasticity in adapting to microenvironmental challenges. Furthermore, cancer cells exhibited substantial perturbation of protein O-glycosylation, leading to simplified glycophenotypes with shorter glycosidic chains. Exploiting glycoengineered cell models, we established that immature glycosylation contributes to reduced cell proliferation and increased invasion. Our findings collectively indicate that hypoxia and glucose deprivation trigger cancer aggressiveness, reflecting an adaptive escape mechanism underpinned by altered metabolism and protein glycosylation, providing grounds for clinical intervention.

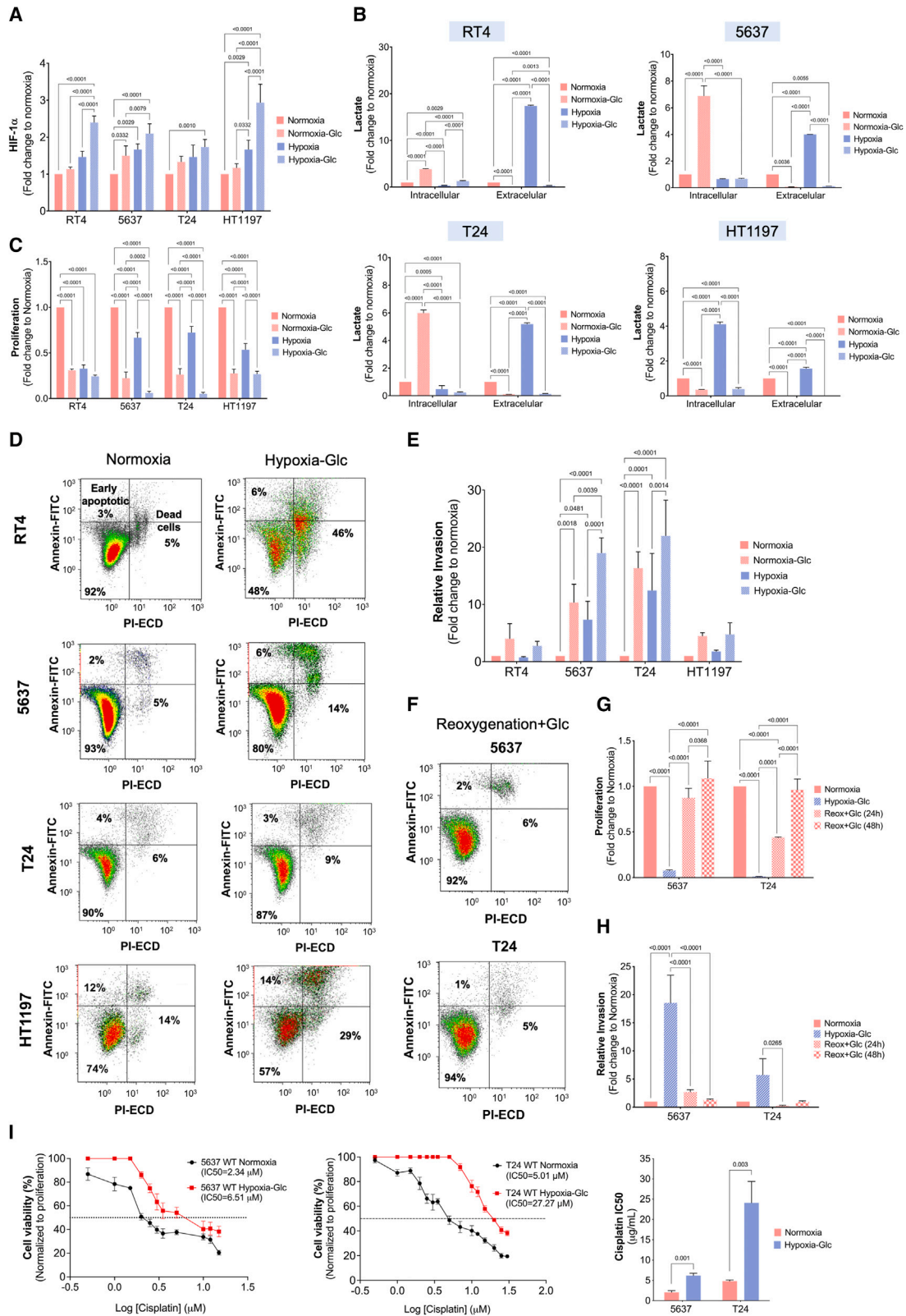
INTRODUCTION

Bladder cancer (BLCA) remains one of the deadliest malignancies of the genitourinary tract due to high intra and inter-tumoral molecular heterogeneity.¹ This has delayed a more comprehensive understanding of tumor spatiotemporal status and affected the efficiency of precise clinical interventions. Although genetic alterations are considered primary causes of cancer development, downstream phenotypic changes induced by the tumor microenvironment are among the driving forces of progression and dissemination. The generation of hypoxic

niches characterized by decreased oxygen availability ($\leq 2\% O_2$) is a microenvironment hallmark of solid tumors.² Not surprisingly, the presence of hypoxic regions is a pivotal independent poor prognosis factor in several cancers, including urothelial carcinomas.³

Uncontrolled tumor cell proliferation supported by avid glucose consumption and glycolysis in the presence of oxygen and fully functioning mitochondria (the Warburg effect) is a common feature of solid tumors.⁴ Rapid proliferation is frequently accompanied by flawed neoangiogenesis, resulting in suboptimal oxygen and nutrient supply to cancer cells in the periphery





(legend on next page)

of blood vessels. Poor vascularization and competition for nutrients require constant metabolic remodeling and exploitation of alternative survival strategies by cancer cells. Although many tumor cells faced with suboptimal growth conditions undergo programmed cell death and necrosis, some subpopulations show tremendous molecular plasticity to adapt to hypoxic and nutrient-deprived microenvironments.⁵ Low oxygen levels induce metabolic rewiring toward anaerobic glycolysis and microenvironment acidification, while contributing to the maintenance of cancer stem cells and acquisition of epithelial-to-mesenchymal transition (EMT) traits, decisively dictating tumor fate.^{6,7} Moreover, slow-dividing cancer cells in hypoxic regions can escape many cytotoxic drugs targeting rapidly dividing cells, also being sufficiently shielded from many other therapeutic agents compared to the tumor bulk.⁸ Although the mechanisms of cellular adaptation to hypoxia are already well known, few studies have interrogated how cancer cells can also withstand low levels of glucose. Furthermore, there is little knowledge of the underlying molecular alterations occurring at the cell surface, which dictate poor prognosis and may be easily targeted in therapeutic interventions.

The cell surface is densely covered by a layer of complex glycans (glycocalyx), which result from the concerted activity of a wide variety of glycosyltransferases, glycosidases, and sugar nucleotide transporters across the secretory pathways.^{9,10} Moreover, glycosylation reflects microenvironmental stimuli in response to alterations in glycoenzyme expression and metabolic imbalances.^{11,12} While aberrant glycosylation, manifested by O-glycans shortening, is a common feature of most epithelial tumors,¹³ there is still a significant gap in identifying the common macroenvironmental drivers responsible for these molecular changes in solid tumors. Nevertheless, seminal observations have linked the Warburg effect with increased flux of glucose and other nutrients into the hexosamine biosynthetic pathway (HBP), resulting in higher mucin-type O-glycosylation and sialylation in cancer cells, directly impacting on glycocalyx composition.^{14,15} These alterations influence the activation of oncogenic signaling, inducing immune tolerance, migration, cell-cell, and cell-matrix adhesion.¹¹ Furthermore, they suggest that meta-

bolic imbalances may play a role in supporting cancer progression by influencing glycocalyx remodeling. Expanding on these findings, a prior explorative study from our group has provided initial evidence that hypoxia augments the malignancy of BLCA cells while concurrently inhibiting protein O-glycosylation extension.¹⁶ However, how hypoxia and glucose restriction shape the cancer glycome and its underlying functional implications remains mostly unaddressed.

In this study, we employed a multi-omics approach combining transcriptomics, metabolomics, glycomics, and phosphoproteomics to characterize in-depth the molecular plasticity of BLCA cells under hypoxia and low glucose and its contribution to aggressiveness. Having observed significant glycome remodeling in response to these stressors, we have conducted functional glycomics studies supported by well-characterized glyco-engineered cell models to determine how altered glycosylation impacts BLCA progression. Important insights were generated to understand how BLCA adapts to oxygen and nutrient deprivation, aiming to identify more aggressive BLCA subpopulations envisaging future clinical interventions.

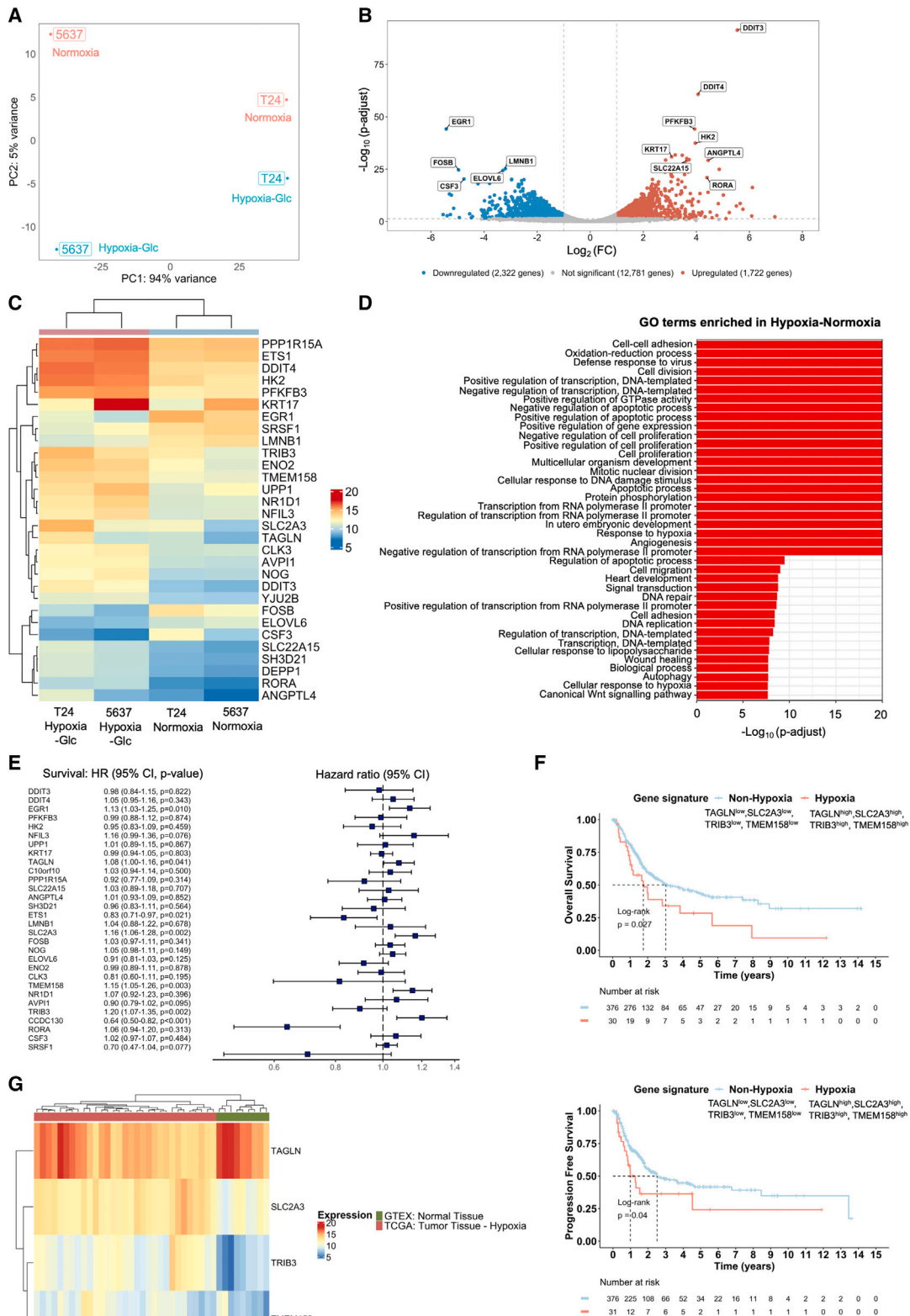
RESULTS

Hypoxia and low glucose induce BLCA aggressiveness

To better understand the molecular adaptability of BLCA cells to hypoxia and low glucose, four BLCA cell models reflecting different grades of the disease (RT4-grade 1, 5637-grade 2, T24-grade 3, HT1197-grade 4) were cultured under low oxygen (0.1% O₂) and reduced glucose ($\leq 10\%$) levels. This was expected to mimic microenvironmental conditions encountered by cells growing far apart from blood vessels.¹⁶ Cells responded rapidly to these challenges, stabilizing the hypoxia-inducible factor HIF-1 α , which became more pronounced in the absence of glucose, supporting HIF-1 α pivotal role in adaptive responses to microenvironmental stress (Figure 1A). Notably, HIF-1 α was also increased in 5637 cells grown under atmospheric oxygen tension but with very low glucose (normoxia-Glc), reinforcing the existence of a non-canonical regulation of HIF-1 α stabilization regardless of oxygen availability.¹⁷ The exception was the

Figure 1. BLCA cells exhibit remarkable tolerance to hypoxia and low glucose, adopting a quasi-quiescent and more aggressive invasive behavior

- (A) Hypoxia or low glucose (normoxia-Glc) significantly upregulates HIF-1 α expression in BLCA cell lines, which is further enhanced when combined (hypoxia-Glc).
- (B) BLCA cells cultured in hypoxia and low glucose produce residual levels of lactate. Individually, these stressors induce the production of lactate.
- (C) Hypoxia and low glucose significantly suppress cell proliferation. Individually, low oxygen or low glucose inhibits cell proliferation. The combination of these stressors further exacerbates this effect in all cell lines.
- (D) BLCA cells maintain their viability under hypoxia and low glucose. The combined environmental stress from hypoxia and low glucose does not significantly impact the viability of 5637 and T24 cells. RT4 and HT1197 cells exhibit a 30%–45% reduction in viability under these conditions, suggesting a limited adaptive capacity.
- (E) BLCA cells display increased invasiveness under hypoxia or low glucose. This is significantly potentiated when both stimuli are combined.
- (F) BLCA cells demonstrate remarkable adaptability to microenvironmental changes with minimal impact on cell viability. Restoring oxygen and glucose levels does not affect cell viability, underscoring the high plasticity of these cells to endure drastic microenvironmental changes.
- (G) BLCA cells restore basal proliferation after 48 h of reoxygenation with glucose restoration. Both 5637 and T24 cells regain proliferative capacity, fully reinstating proliferation after 48 h, highlighting their plasticity in responding to microenvironmental challenges.
- (H) After 24 h of reoxygenation with glucose restoration, BLCA cells exhibit a significant reduction in invasion, which is fully restored under normoxia after 48 h.
- (I) Hypoxia and low glucose increase T24 cells' resistance to cisplatin across a wide range of concentrations, including its IC₅₀, whereas 5637 cells remain unchanged. Error bars represent mean \pm SD for three independent experiments. One-way ANOVA followed by Tukey's multiple comparison test and the Mann-Whitney test were used for statistical analysis. Results were considered statistically significant when $p < 0.05$.



(legend on next page)

T24 cell line, which showed a modest HIF-1 α increase under stress, even though nuclear accumulation was notorious in subsequent experiments. This was accompanied by an increase in lactate levels, which were rapidly extruded to the extracellular space under low oxygen (Hypoxia), suggesting the adoption of anaerobic glycolysis as main bioenergetic pathway and capacity to maintain intracellular homeostasis⁷ (Figure 1B). Low glucose (normoxia-Glc) also increased lactate as a result of aerobic glycolysis, except for HT1197 cells. However, it remained in the intracellular compartment, suggesting that low oxygen may be critical for activating extrusion mechanisms. Under these conditions, lactate may be converted into pyruvate to fuel the Krebs cycle. The combined effect of hypoxia and low glucose (Hypoxia-Glc) lowered lactate close to vestigial levels, strongly supporting the activation of an alternative energy-producing pathway to glycolysis.

Concomitantly, we observed a striking decline in cell proliferation (approximately 1.5-fold) in all cell lines under hypoxia, which was significantly enhanced upon glucose suppression (Figure 1C). Cells were arrested in G2/M checkpoint, most likely due to depletion of the substrates required for DNA synthesis, as it was later confirmed by metabolomics (Figure S1). Notably, the viability of 5637 and T24 cells was not affected after 24 h of microenvironmental stress, as highlighted by little changes in the percentage of apoptotic and pre-apoptotic cells in comparison to normoxia (Figure 1D). Expanding this study, we found that 5637 and T24 were even able to withstand these stressors for at least 72 h without loss of cell viability, demonstrating their significant adaptability. In contrast, RT4 and HT1197 cells viability was decreased by approximately 30%–50% after 24 h. As such, 5637 and T24 cells were selected for more in-depth functional and molecular studies. After 24 h, 5637 and T24 cells responded to oxygen or glucose shortage by increasing invasion of Matrigel *in vitro* (Figure 1E). Strikingly, their combination (hypoxia-Glc) enhanced further invasion, highlighting the pivotal role played by both stressors. Finally, reoxygenation and access to glucose restored proliferation after 24 h and induced a massive drop in invasion without inducing apoptosis, suggesting little oxidative stress from drastic alterations in the microenvironment (Figures 1F–1H). Collectively, this demonstrated that certain

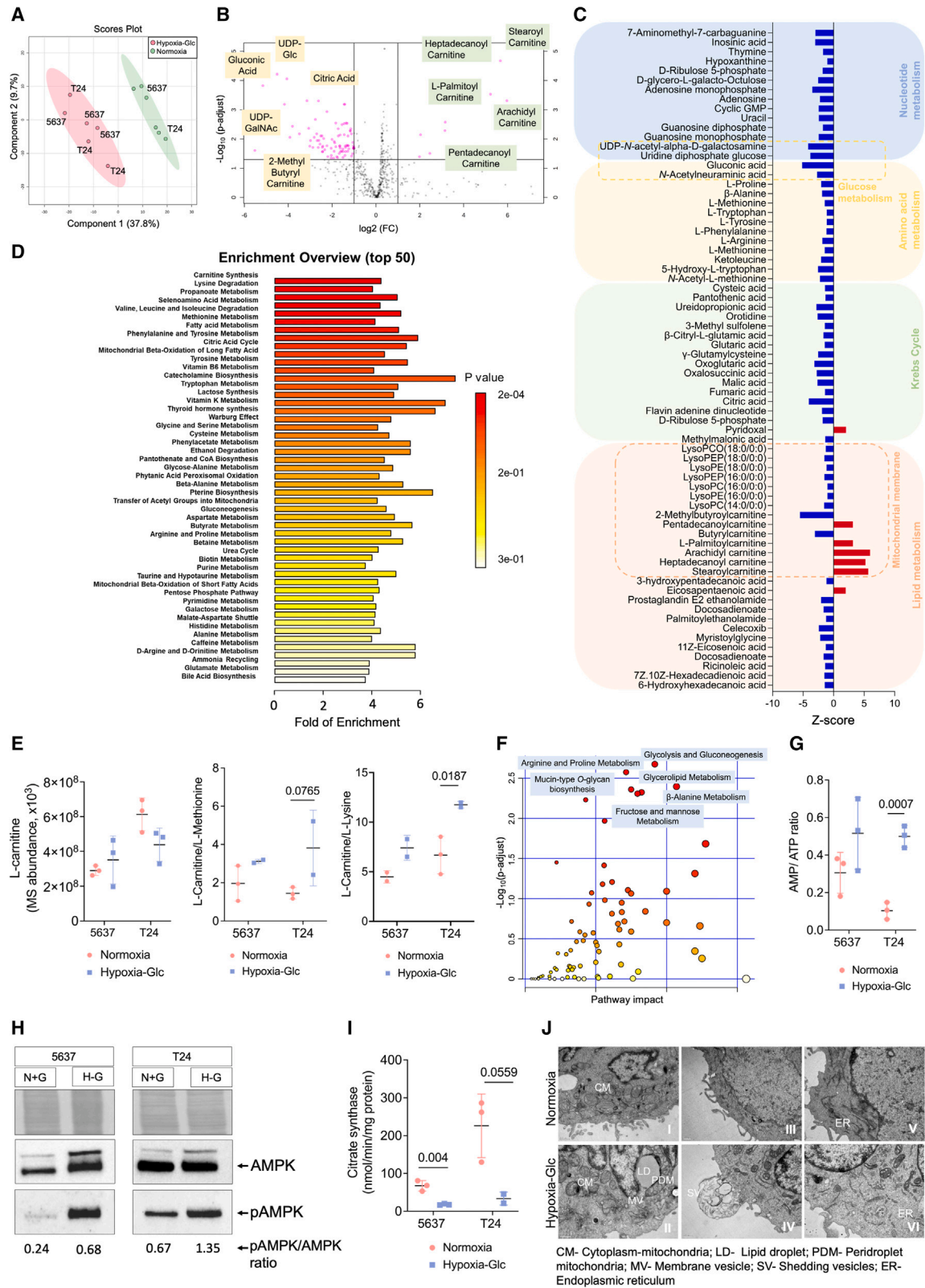
BLCA cell subpopulations are well capable of accommodating hypoxia-induced stress, while concomitantly acquiring more aggressive and motile phenotypes. Overall, our results suggest that oxygen and glucose levels act as an on-off switch for proliferation and invasion. Interestingly, resistance to cancer cell death, proliferation decline, and activation of invasion traits have been closely linked to lactic acidosis as a result of either hypoxia or glucose shortage.⁷ Our observations support the adoption of similar behaviors in the absence of lactate. Finally, we addressed 5637 and T24 tolerance to cisplatin, generally used in the clinics against less proliferative tumor cells. Under stress, BLCA cells significantly increased tolerance to cisplatin as observed for T24 and 5637 cells (Figure 1I), suggesting the adoption of cell chemoresistance mechanisms, which could be directly related to decreased proliferative potential promoted by stress conditions.

Stress-induced transcriptome rewiring supports cancer aggressiveness and metabolic reprogramming

The 5637 and T24 BLCA cells showed markedly different transcriptomes but common responses to hypoxia and glucose shortage (Figure 2A). A total of 4,044 genes were differentially expressed in response to stress (1,722 upregulated, 2,322 downregulated; Figure 2B and Tables S1 and S2), thus supporting significant transcriptome remodeling. Under hypoxia and glucose deprivation, cells activated stress-related genes driving more undifferentiated (*KRT17*),¹⁸ poorly proliferative (*PPP1R15A/GADD34*)¹⁹, and cell-death-resistant (*PPP1R15A/GADD34*,²⁰ *DDIT4*,²¹ *PFKFB3*)²² phenotypes (Figure 2C). Furthermore, upregulation of *DDIT4*, *HK2*, *PFKFB3*, and *PPP1R15A/GADD34* supported the activation of autophagic events.^{23–26} In particular, *PPP1R15A/GADD34* plays a key role in sustaining autophagy during starvation, thus enabling lysosomal biogenesis and a sustained autophagic flux,²⁶ whereas *DDIT4* has been linked to adaptive survival mechanisms permitting cells to resist metabolic stress.²⁷ Finally, we observed significant downregulation of genes linked to lipogenesis (*ELOVL6*),²⁸ as well as both proliferation and positive regulators of differentiation (*FOSB*, *CSF3/G-CSF*).^{29–31} Furthermore, hypoxia and low glucose levels negatively regulated tumor suppressors (*EGR1*)³² and activated

Figure 2. BLCA cell lines under hypoxia and low glucose experience profound transcriptome remodeling, linked to the acquisition of more aggressive phenotypes, which is supported by the poor prognosis observed in TCGA-BLCA patients

- (A) BLCA cell lines under hypoxia and low glucose display distinct transcriptomes but share common responses to these conditions. PCA for transcriptomics data reveals that PC1 (94% variance) primarily distinguishes differences between cell lines, whereas PC2 (5% variance) highlights marked changes between normoxic and stressed cells.
- (B) The volcano plot showcases global transcriptional changes between normoxia and hypoxia plus low glucose. Exposure to these stressors alters the expression of 4,044 genes (1,722 upregulated, 2,322 downregulated), indicating significant transcriptome remodeling.
- (C) Bi-clustering heatmap of the top 30 differentially expressed genes illustrates co-regulation under stress, supporting proliferation arrest, resistance to cell death, and invasion. Heatmap plots log₂ transformed expression values of genes in samples.
- (D) Enrichment analysis of GO terms for differentially expressed genes reveals alterations in key pathways associated with cell-cell adhesion, cell proliferation, and resistance to cell death.
- (E) Prognostic evaluation identifies a hypoxia and glucose-deprivation-linked four-gene signature (*TAGLN*^{high}; *SLC2A3*^{high}; *TRIB3*^{high}; *TMEM158*^{high}). Univariate Cox regression analysis of the top 30 differentially expressed genes identifies seven genes associated with OS. Higher expression levels of four genes, upregulated under hypoxia and low glucose, significantly correlate with poor OS, constituting a stress signature.
- (F) Validation of the prognosis significance of the hypoxia-related four-gene signature in BLCA patients from TCGA. Kaplan-Meier curves of OS and PFS show significantly worse clinical outcomes for patients displaying the stress-related gene signature compared to the remaining patients in the cohort.
- (G) Bi-clustering heatmap showing the association between the stress-related signature and bladder tumors. Heatmap plots log₂ transformed expression values of the four hypoxia-related differentially expressed genes, showing clear differentiation between cancer and healthy bladder samples.



(legend on next page)

genes linked to invasive/migratory capacity (*ETS1*,³³ *DDIT4*,³⁴ *TAGLN*,³⁵ *TMEM158*³⁶). Collectively, BLCA cells showed remarkable transcriptomic adaptability to microenvironmental stress, supporting increased cancer aggressiveness. Genes involved in cell-cell adhesion, cell proliferation, programmed cell death, DNA damage, metabolism reprogramming, and oxidation-reduction processes (Figure 2D) were triggered, in accordance with the observed functional alterations (Figure 1). The transcriptome of bladder tumors ($n > 400$ cases) showed significant correlation with hypoxia-related genes observed in stressed cell lines (Figure S2). Moreover, a distinct hypoxic phenotype (characterized by *TAGLN*, *SLC2A3*, *TRIB3*, and *TMEM158* upregulation) was identified in more aggressive tumors and associated with a worse prognosis (Figures 2E and 2F). Importantly, this hypoxic phenotype was discriminative of tumors compared to healthy tissues (Figure 2G).

Microenvironmental stress induces catabolic metabolism

To gain more insights into the metabolic reprogramming induced by hypoxia and glucose deprivation, we performed a mass-spectrometry-based untargeted metabolomics study on 5637 and T24 cells (Tables S3 and S4). As highlighted by Figure 3A, T24 and 5637 cells present distinct metabolic fingerprints under normoxia, in line with the different molecular backgrounds observed at the transcriptome level (Figure 2). However, similar responses were observed facing low oxygen and glucose, characterized by a statistically significant reduction in the levels of 85 metabolites and increments in 8 species. Increased metabolites included several fatty acid-carnitine derivatives, whereas nucleotide sugar donors (UDP-Glc and UDP-GalNAc), citric acid, and gluconic acid were substantially decreased (Figures 3B and 3C). High levels of fatty acid-carnitine derivatives (pentadecanoylcarnitine, L-palmitoylcarnitine, heptadecanoyl carnitine, stearoyl carnitine, arachidyl carnitine; Figures 3B and 3C) support active translocation of long-chain fatty acids across the inner mitochondrial membrane for subsequent β -oxidation. Interestingly, increased levels of these metabolites have been observed in the urine of advanced-stage BLCA patients,^{37,38} reinforcing the close link between this metabolic phenotype and cancer aggressiveness.

In addition, stressed cells showed decreased amounts of several lysophosphatidylcholines and lysophosphatidylethanolamine, which is consistent with the mobilization of lipids for mitochondrial β -oxidation³⁹ (Figure 3C) and in perfect agreement with the lipolytic phenotype highlighted by transcriptomics. Interestingly, carnitine levels were also conserved to maintain downstream lipid β -oxidation at the expenses of L-lysine and L-methionine degradation (Figures 3C–3E). On the other hand, stressed cells showed significant amounts of Krebs cycle intermediates, namely citrate, but also oxoglutarate, oxaloacetate, malate, and fumarate. Interestingly, lower citrate in cancer cells has been described to favor resistance to apoptosis and cellular dedifferentiation,⁴⁰ thus in agreement with functional and transcriptomics studies. Of note, we also observed amino acids consumption (lysine, valine, leucine, isoleucine; Figure 3D) to support energy requirements. A joint pathway analysis, combining transcriptomics, and metabolomics confirmed the molecular re-wiring of challenged cells toward a catabolic state (Figure 3E). It further highlighted changes in glycolysis and gluconeogenesis, in agreement with the adoption of a lipolytic rather than a glycolytic metabolism.

Not surprisingly, we found a higher AMP/ATP ratio in stressed cells (Figure 3G), mainly driven by a significant decrease in ATP. This was accompanied by higher 5-AMP-activated protein kinase (AMPK) phosphorylation (Figure 3H), frequently observed in more aggressive bladder tumors.⁴¹ These findings were both consistent with the adoption of catabolic processes and supported the occurrence of mitophagy. Accordingly, microenvironment-challenged cells displayed decreased citrate synthase activity (Figure 3I) and higher number of autophagosomes (Figure S3A). Autophagy in hypoxic cells was confirmed by dedicated immunoassays (Figure S3B). Mitophagy was also later confirmed by TEM (Figure 3J). In fact, microscopy evidenced a drastic decrease in the number of intact mitochondria, allied to evident mitophagy events (Figures 3J I and II), translated by outer mitochondrial-membrane-associated degradation and matrix sectioning. Lipid-droplet (LD)-associated mitochondria, also known as peridroplet mitochondria (PDM), were also observed under hypoxic conditions (Figures 3J III). Vesicle shedding was evident (Figures 3J III and IV), highlighting cellular communication

Figure 3. Hypoxia and low glucose shift BLCA cell metabolism from glycolytic to lipolytic, increasing lipid droplet formation and reducing the number of active mitochondria

(A–C) PLS-DA analysis reveals similar metabolic responses in 5637 and T24 cells under microenvironmental stress (A). Volcano plot highlights significant metabolome alterations in response to hypoxia and low glucose (B). Downregulated metabolites include UDP-Glc, UDP-GalNAc, gluconic acid, and citric acid, whereas increased metabolites indicate active fatty acid transport and β -oxidation (C). Significant reduction in key metabolites linked to nucleotide, amino acids, Krebs cycle, and lipid metabolism was observed, consistent with catabolic metabolism. An exception is the accumulation of long fatty acid acylcarnitine for transfer across the inner mitochondrial membrane for β -oxidation.

(D) Pathway enrichment analysis supports fatty acid β -oxidation as the primary bioenergetic pathway in stressed cells. Key metabolic pathways, including carnitine biosynthesis and lysine/methionine degradation, contribute to fatty acid β -oxidation.

(E) Hypoxia and low glucose induce lysine and methionine degradation to support acylcarnitine biosynthesis and lipid β -oxidation.

(F) Joint pathway analysis incorporating transcriptomics and metabolomics studies supports changes from glycolytic to lipolytic metabolism, impacting nucleotides and sugars biosynthesis, including O-GalNAc glycans and protein O-glycosylation.

(G and H) Hypoxia and low glucose increase AMP/ATP ratio (G) and activate AMPK by phosphorylation (H), indicating impaired oxidative phosphorylation and potential catabolic processes, including mitophagy.

(I) Citrate synthase activity decreases under hypoxia and low glucose, suggesting a reduction in functional mitochondria.

(J) TEM analysis reveals major morphological changes, including compromised mitochondria, lipid droplets, peridroplet mitochondria, membrane vesicles, and increased shedding of vesicles, indicating membrane activity changes under stress. Error bars represent mean \pm SD for three independent experiments. Mann-Whitney test was used for statistical analysis. Results were considered statistically significant when $p < 0.05$.

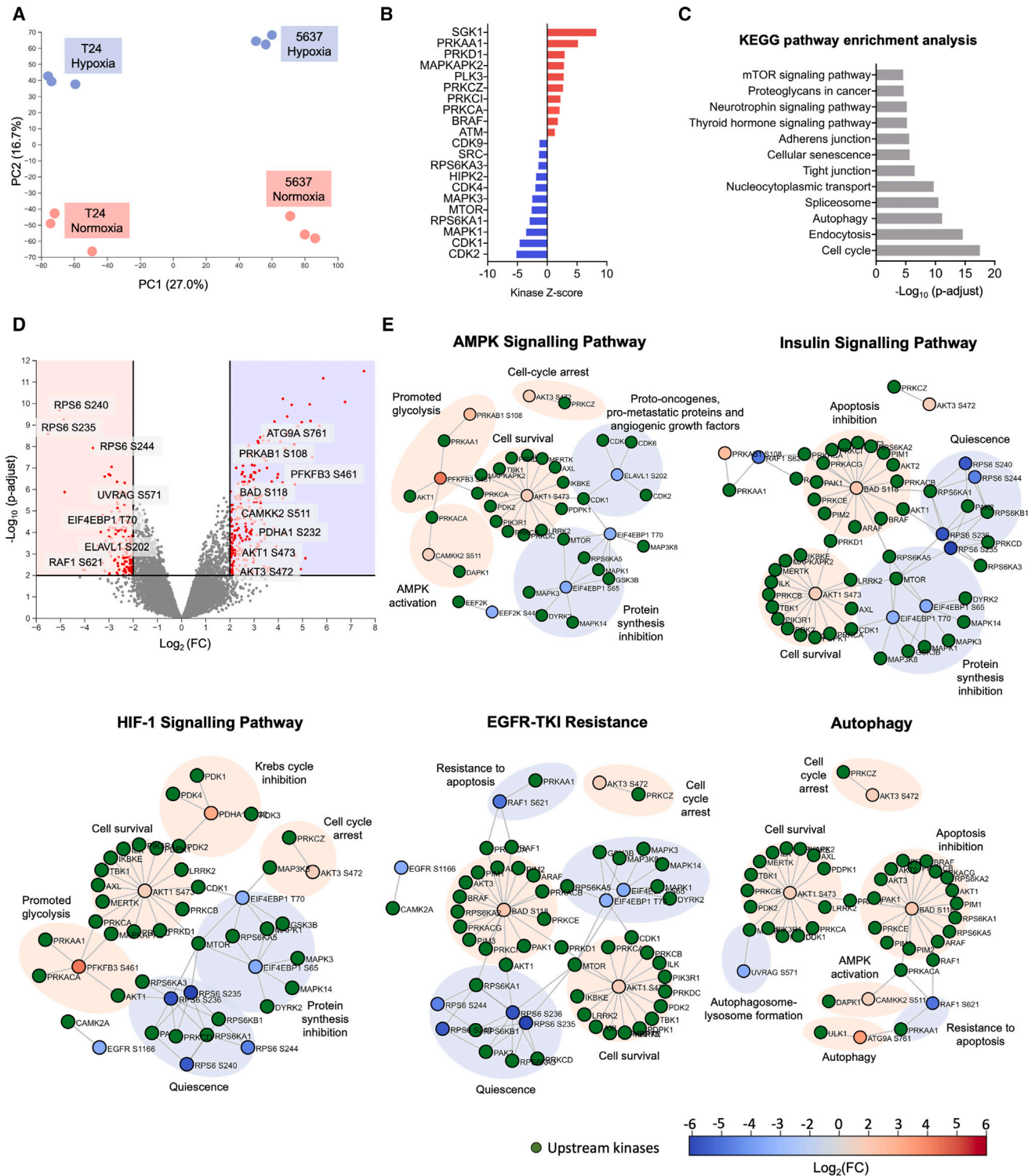


Figure 4. Hypoxia and low glucose induce major cell signaling rewiring, promoting aggressiveness via cell-cycle arrest, quiescence, apoptosis resistance, glycolytic metabolism blockage, and autophagy

(A) Despite cell-related differences, common features in oncogenic signaling are elicited by hypoxia and glucose deprivation, as shown by PCA analysis of phosphoproteome signatures. PC1 (27% variance) distinguishes cell-dependent differences, whereas PC2 (17% variance) relates to marked signaling changes linked to hypoxia and glucose deprivation.

(legend continued on next page)

events that should be carefully investigated in future studies. Finally, stressed cells showed considerably short and disorganized endoplasmic reticulum (ER) cisternae, contrasting with typically longer ER sections presented by cancer cells in normoxia (Figures 3JV and VI), demonstrating prominent disorganization of secretory pathways where glycosylation occurs (Figure S4). Overall, cellular ultrastructure was significantly altered in ways that are consistent with catabolic responses leading to lipid droplets accumulation and disorganization of major organelles linked to glycosylation. Therefore, we further investigated alterations in the ER and Golgi apparatus (GA) proteomes under hypoxia and glucose restriction (Figures S5A and S5B). ER-related proteins FKBP2, HYOU1, HSP90B1, ERO1A, and HSPA5 were significantly increased, and SDF4 was decreased in both cell lines (Figure S5A). This highlights common unfolded protein responses intricately linked to ER stress, including organelle fragmentation and functional impairment.^{42–45} Regarding the Golgi, we found that GOLM1 was also decreased in both cell lines (Figure S5B). GOLM1 plays a pivotal role assisting in the transportation of protein cargo through the Golgi apparatus.⁴⁶ Overall, ER and GA proteome remodeling supports the adoption of stress-counteracting responses and negative regulation of apoptosis, as evidenced by the functional network in Figure S5C. Collectively, proteomic findings reinforce TEM evidence of impairment in secreting organelles.

Cellular signaling rewiring under stress supports aggressiveness

Cellular signaling rewiring was assessed by phosphoproteomics (Tables S5 and S6). Under stress, 5637 and T24 BLCA cells responded similarly (Figure 4A), exhibiting major alterations in relevant serine/threonine kinases and substrates linked to high motility and reduced cell adhesion, reduced cell proliferation, cell senescence, and mitochondrial reorganization (Figures 4B and 4C; Tables S5 and S6). Moreover, cells exhibit clear survival adaptations translated by induction of autophagy, apoptosis evasion, cell-cycle arrest, Krebs cycle inhibition, and cell survival (Figure 4), in full agreement with functional, transcriptome, and metabolome reprogramming. Increased endocytosis was also a relevant feature of these cells, supporting major plasma membrane remodeling observed by TEM. Notably, the most significant alterations in phosphorylation (>2-fold change to normoxia) occurred in proteins involved in the AMPK, insulin, HIF-1 α , EGFR tyrosine kinase, and autophagy signaling pathways (Figure 4E). The main altered phosphorylation sites under hypoxic conditions are AKT1 S473, AKT3 S472, PFKFB3 S461, CAMKK2 S511, PDHA1 S232, BAD S118, and PRKAB1 S108 (Figure 4D; Tables S5 and S6). AKT1 S473 and AKT3 S472 act synergically

to protect cells from microenvironmental and cisplatin-induced apoptosis by phosphorylating downstream molecules as mTOR and glycogen synthase kinase-3. Notably, under stress, the preferable PRKCZ substrate is AKT3 whose activity was found significantly increased (Figure 4E). PRKCZ has been implicated in maintaining high motility and reduced cell adhesion of metastatic cancer cells,⁴⁷ in cell-cycle regulation,⁴⁸ and in mitochondrial reprogramming in senescent cells toward cell survival. Also, BAD apoptotic activity is attenuated by phosphorylation at S118, precluding binding to other Bcl-2 family members to evade apoptosis.⁴⁹ Furthermore, phosphorylated PDHA1 at S232 inactivates pyruvate dehydrogenase complex,⁵⁰ redirecting cells toward alternative energy pathways to Krebs cycle. Together with elevated phospho-PRKAB1 S108, this is consistent with the adoption of catabolic processes such as fatty acid β -oxidation and potential mitophagy⁵¹ sustained by AMPK activation (Figures 4D and 4E). A significant decrease in several forms of RPS6 (S240, S235, S244), RAF1 S621, ELAVL1 S202, and EIF4EBP1 T70 is also compatible with impaired cancer cell proliferation observed under stress.^{52–55} These alterations are consistent with the adoption of more aggressive phenotypes by microenvironment-challenged cells.

Stress induces an immature glycolyx

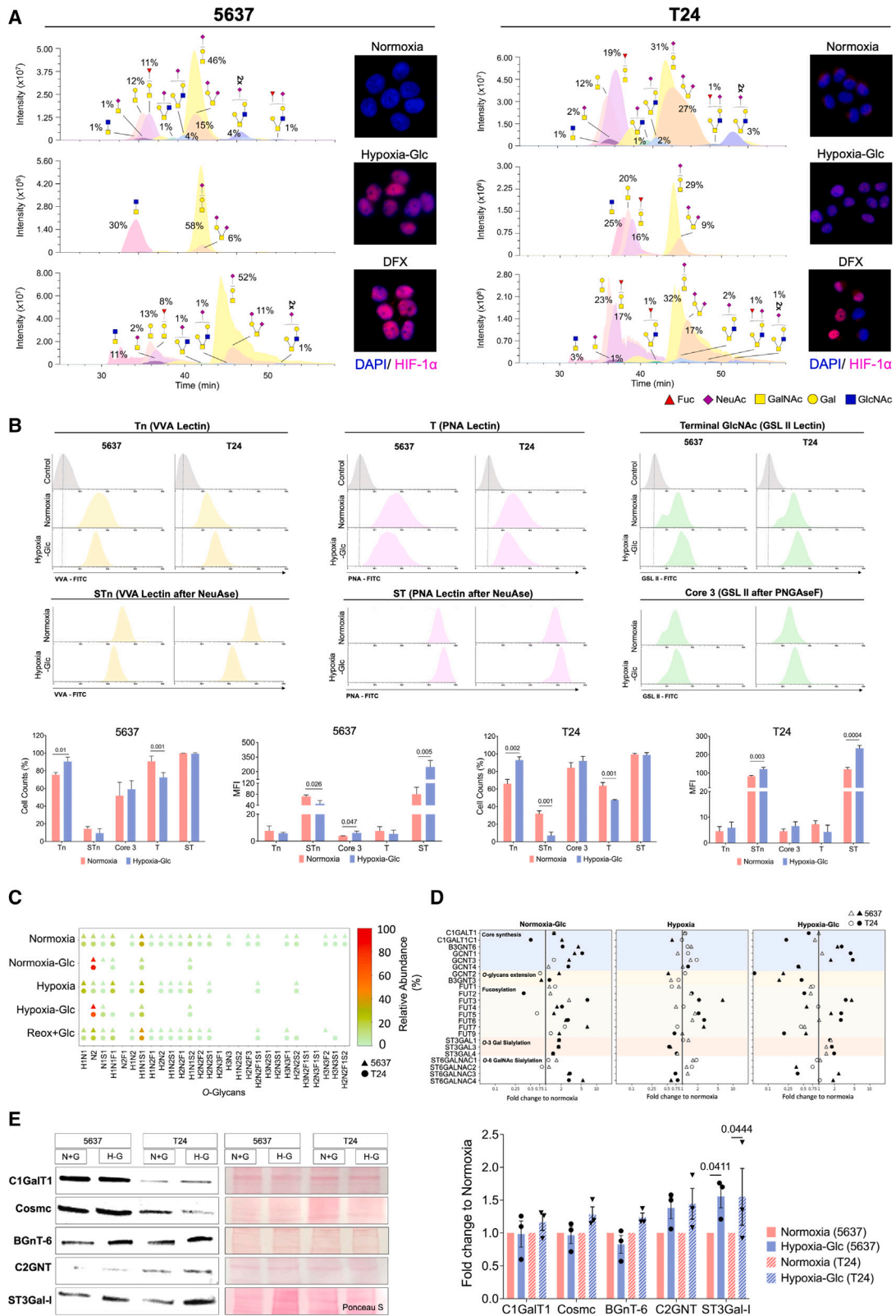
The generalized disorganization of secretory organelles on stressed cells strongly suggests implications for the cells' glycolyx. In addition, Figure 3 supports major alterations in glycosylation pathways driven by changes in metabolites linked to glycosylation. This includes UDP-GalNAc, a key sugar nucleotide for the initiation of protein O-GalNAc glycosylation and Neu5Ac, a sialic acid capping different glycoconjugates (Figures 3C and S4). Data also suggest low flux through the hexosamine pathway, which impacts UDP-GlcNAc biosynthesis required for glycosylation, even though this metabolite could not be detected by our approach. We further observed decreased UDP-Glc, which is a key precursor of UDP-Gal and UDP-GlcA needed for glycoproteins, proteoglycans, and glycolipids glycosylation. Finally, lower levels of gluconic acid and D-ribulose 5-phosphate as well as AMP, UMP, GMP, and GDP demonstrate alterations in the pentose phosphate pathway (Figures 3C and 3D) required to generate nucleotides for nucleic acid synthesis but also glycosylation. Major inhibition of mucin-type O-GalNAc glycans biosynthesis as well as fructose and mannose metabolism required for glycosylation was also evident in the joint pathway analysis (Figure 3E). In addition, downregulation of several glyco-genes encoding polypeptide *N*-acetylgalactosaminyltransferases responsible for protein O-glycosylation initiation (Table S7) was evident from transcriptome analysis. Downregulation

(B) Kinase-substrate enrichment analysis scores each kinase based on substrate phosphorylation, highlighting major alterations in stressed cells. Red indicates significantly activated kinases, whereas blue indicates significantly inhibited ones (Z score ≥ 2 or ≤ -2).

(C) KEGG pathway enrichment analysis of phosphoproteomics data shows significant alterations in cell signaling pathways supporting cell motility, cellular senescence, and autophagy under stress.

(D) Volcano plot showcases global cell signaling rewiring between normoxia and hypoxia plus low glucose, indicating the most significantly hyper- or hypo-phosphorylated proteins and precise annotation of main phosphorylation sites.

(E) AMPK, insulin signaling, HIF-1 α signaling, EGFR-TKI resistance, and autophagy are the most significantly altered pathways in stressed cells. Top-ranked signaling pathways with 2-fold change in stressed cells are presented, highlighting the most significant hyper- or hypo-phosphorylated proteins and precise phosphorylation sites, along with main associated cellular functions.



(legend on next page)

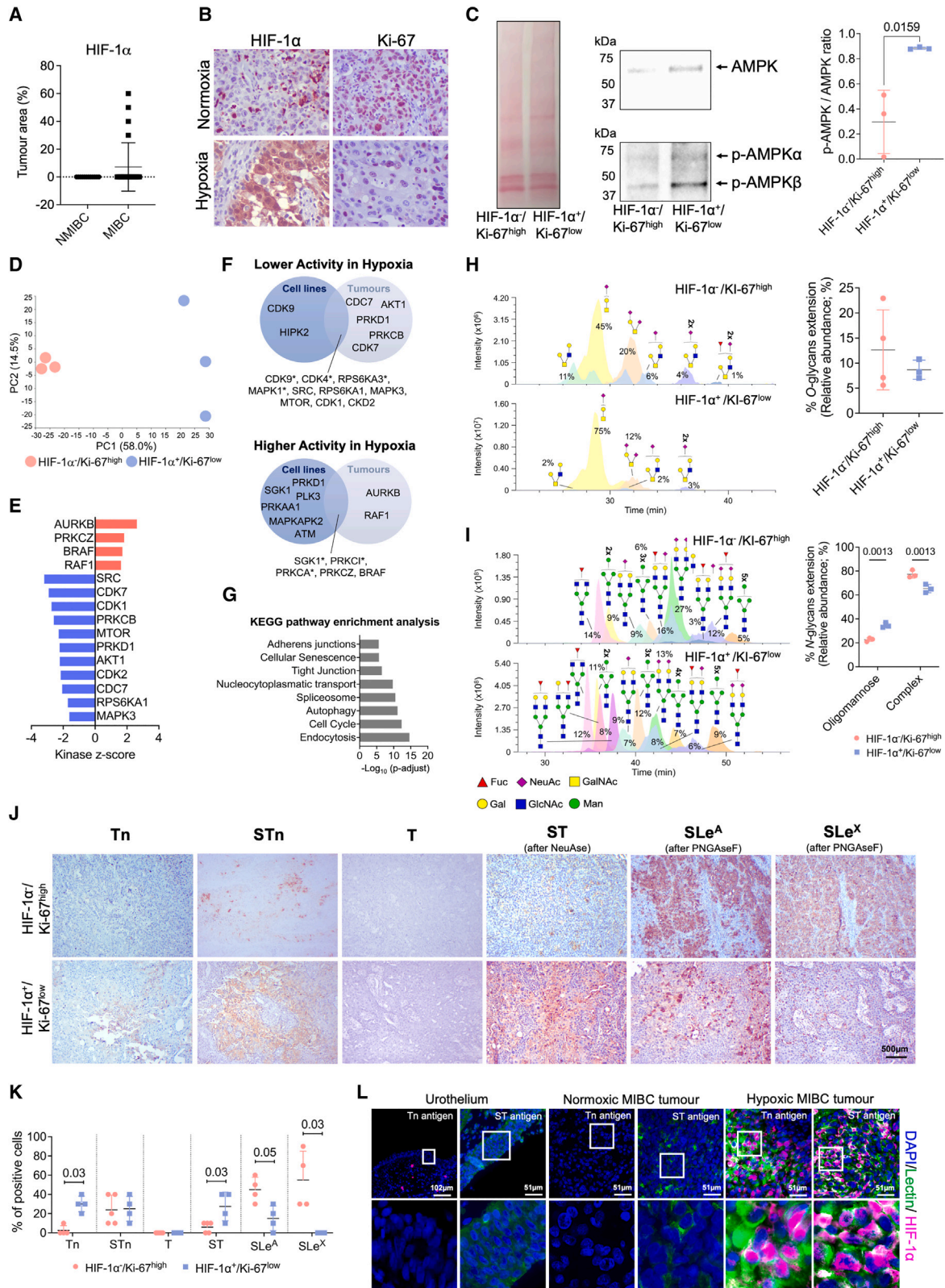
of *C1GALT1C1*, encoding an essential chaperone for core 1 *O*-glycan T-synthase activity and further *O*-glycans elongation, was also observed. Interestingly, stressed cells also presented downregulation of key glycosyltransferases for early *N*-glycans processing in the ER but also *N*- and *O*-glycans elongation in the Golgi. Finally, we observed downregulation of several glyco-genes linked to proteoglycans biosynthesis (Table S7). In summary, the disorganization of secretory organelles and decreased sugar nucleotides, accompanied by a net downregulation of key glyco-genes linked to glycosylation initiation and elongation, drive an immature glyco-phenotype.

Building on our previous studies linking immature glycosylation with BLCA aggressiveness, we devoted to the precise characterization of the *O*-GalNAc glycome of stressed cells. This was performed by exploiting the Tn mimetic benzyl- α -GalNAc as a scaffold for further *O*-chain elongation, providing a good assessment of *O*-glycosylation pathways fitness (Figures 5 and S4; Table S8). According to Figure 5A, low oxygen and glucose significantly reduced *O*-glycans synthesis in both cell lines (Figure S6 and Table S8). More detailed glycomic characterization in Figure 5C showed that both cell lines abundantly express fucosylated (m/z 746.40; H1N1F1; type 3 H-antigen) and sialylated T (m/z 933.48; H1N1S1) antigens, also exhibiting several extended core 2 *O*-glycans of variable lengths and degrees of fucosylation and sialylation. Low amounts of shorter *O*-glycans such as core 3 (m/z 613.33; N2) and STn (m/z 729.38; N1S1) antigens could also be observed. Complementary flow cytometry analysis using lectins (VVA for Tn; VVA after NeuAse for STn; PNA for T; PNA after NeuAse for STn; and GSL II after PNGase F for terminal GlcNAc) was employed to gather semi-quantitative data on most relevant glycan structures (Figure 5B). This was particularly relevant for estimating the Tn antigen, which could not be directly assessed by the adopted MS methodology. Accordingly, 60%–80% of the cells originally expressed Tn, whereas only 15%–30% expressed STn. The reduction of oxygen and glucose significantly impacted the glycome of cells, inducing a more homogeneous simple cell glyco-phenotype characterized by few short-chain *O*-glycans without chain extension beyond core 2, mainly mono- (m/z 933.48; H1N1S1) and, to less extent, di-sialylated (m/z 1294.65; H1N1S2) T antigens and core 3 (N2) (Figures 5A–5C). Under hypoxia and glucose deprivation, STn (N1S1) expression remained negligible as few cells express

this glycan (>10% of the cells) (Figure 5B). Interestingly, no extension of pre-existing core 3 was observed, reinforcing the inexorable expression of shorter structures by stressed cells. Furthermore, we found that the main driver for the lack of glycan extension was the reduction in glucose (Figure 5C). Notably, BLCA cells regained the capacity to extend glycans after reoxygenation and reintroduction of glucose (Figure 5C), demonstrating significant plasticity and that microenvironmental stressors act as an on-off switch for *O*-glycosylation. Complementary flow cytometry studies showed that the percentage of cells expressing T antigen decreased under hypoxia and glucose deprivation in comparison to normoxia, whereas the abundance of sialylated T antigens was significantly increased (Figure 5B). Also, the percentage of Tn-expressing cells increased under stress, whereas STn levels remained residual, as most Tn antigen is maintained in its non-sialylated form. Overall, these findings highlight that *O*-glycosylation extension is antagonized under hypoxia and glucose deprivation, leading to more homogeneous glyco-phenotypes with accumulation of shorter *O*-glycans. Interestingly, we found similar patterns in a wider panel of cell lines, including RT4 and HT1197, but also esophageal, gastric, and colorectal cancer cells and human monocyte-derived macrophages (Figure S7 and Table S9), suggesting common response patterns to stress by cancer cells and normal immune cells. Notably, in these cells, core 2 was significantly decreased but not completely lost. Finally, we exposed BLCA cells to deferoxamine (DFX), an iron chelator known to stabilize HIF-1 α expression, and confirmed nuclear accumulation of HIF-1 α (Figure 5A). Upon exposure to DFX, both cell lines exhibited a significant decrease in the expression of *C1GALT1C1*, a crucial glycosyltransferase responsible for *O*-chain elongation beyond the Tn antigen. Additionally, in 5637 cells, *GCNT1*, which regulates core 2 biosynthesis, is downregulated, whereas T24 cells upregulate *ST3GAL1* (Figure S8). These alterations could potentially contribute to a premature stop in glycans elongation. Interestingly, DFX did not induce significant changes in the glycosylation of both cell lines, indicating that the HIF-1 α transcription factor might not exert a major influence on glycome remodeling, despite its role in regulating crucial *O*-glyco-genes expression. Our observations also highlight the need for careful interpretation of the glycome based on glyco-genes expression. Finally, seeking deeper insights on the relation between

Figure 5. Hypoxia and low glucose impair *O*-glycans extension in BLCA, originating a simple cancer cell glyco-phenotype

- (A) BLCA cells exposed to hypoxia and low glucose exhibit less abundant, simpler, and shorter glycomes, lacking extensions beyond core 1 structures. nanoLC-MS/MS analysis shows that this glyco-phenotype is characterized by sialylated T antigens and core 3, likely due to decreased typical core 1 and 2 structures. DFX-treated cells, stabilizing HIF-1 α , show no significant alterations in the glycome, suggesting that changes observed in stressed cells are not driven by HIF-1 α .
- (B) Lectin affinity studies show significant upregulation of Tn and sialylated T antigens (recognized by PNA lectin after Neuraminidase [NeuAse] digestion) under stress, in accordance with MS-based glycomics. Notably, core 3 *O*-glycans (evaluated by GSL II lectin after PNGase F digestion) remain unchanged, highlighting that cellular stress primarily suppresses core 1/2 *O*-glycans, rather than increasing core 3 *O*-glycans.
- (C) Glucose suppression is the primary driver of glycome remodeling, which can be reversed by reoxygenation and restoration of glucose.
- (D) Glycome remodeling is primarily driven by the combined effects of hypoxia and glucose deprivation and leads to a premature halt in glycans extension beyond core 1. *C1GALT1C1*, necessary for core 1 biosynthesis, is downregulated, whereas *ST3GAL1*, 3, and 4 are overexpressed, increasing sialylated T antigens and inhibiting core 2 formation. Downregulation of *GCNT4* also contributes to core 2 inhibition. Interestingly, elevated *GCNT1* and *GCNT3* potentially counterbalance core 2 suppression.
- (E) Quantification of key enzymes involved in *O*-glycan elongation (*C1GalT1*; *Cosmc*; *BGNt-6*; *C2GNT*; *ST3Gal-I*) shows significant upregulation of *ST3Gal-1* in stressed cells, consistent with transcriptomics. The others remain unchanged, indicating distinct regulation between glyco-genes and glycosyltransferases under these conditions. Bold circles and triangles represent statistically significant changes in T24 and 5637 cell lines, respectively. Error bars represent mean \pm SD for three independent experiments. Mann-Whitney Test was used for statistical analysis. Results were considered statistically significant when $p < 0.05$.



(legend on next page)

glycogenes expression and the glyco-phenotype, we re-analyzed by RT-PCR the expression of a wide array of glycosyltransferases involved in the initial steps of O-glycans biosynthesis (Figure 5D). Glucose suppression impacted more significantly glycogenes expression than hypoxia, inducing significant overexpression of glycosyltransferases linked to O-glycans elongation, namely *C1GALT1*, *C1GALT1C1* (for T24 cells), *GCNT1*, and *B3GNT6*, but also extension and termination by fucosylation and/or sialylation (Figure 5D). *ST3GAL1* overexpression was observed and may contribute to a premature stop in core 1 extension by O-3 sialylation, decreasing core 1 fucosylation. Interestingly, the combination of both hypoxia with low glucose impacted less on glycogenes remodeling than glucose suppression alone (normoxia-Glc). Notably, *B3GNT6* and *ST3GAL1* remained overexpressed (Figure 5D). Downregulation of *C1GALT1* and *C1GALT1C1* was also observed (Figure 5D), which may contribute to reduced core 1 synthesis and further elongation to core 2, impacting negatively on glycans extension. However, western blot analysis showed that, despite changes in glycogenes expressions, ST3Gal-I was the only main glycosyltransferase gatekeeper of O-glycans extension found elevated in stressed cells. (Figure 5E). Also, while the focus was set on O-GalNAc glycosylation, we also characterized the N-glycome. Despite changes in N-glycogenes expression (Table S7), no major alterations could be observed in relation to the main types of N-glycans (oligomannose, paucimannose, complex; Table S10).

Hypoxic bladder tumors share common molecular features with stressed cell lines

We then assessed the translational character of our observations in patient samples. A cohort of BLCA surgical tissue sections without prior history of adjuvant treatments ($n = 70$), comprehending non-muscle (NMIBC; $n = 30$) and muscle invasive (MIBC; $n = 40$) tumors spanning all stages of the disease (Ta, T1, T2, T3, T4), was elected for this study. The tumors were screened for nuclear expression of HIF-1 α and expression of the proliferation marker Ki-67 (HIF-1 α ⁺ Ki-67^{low}; hypoxic phenotype). HIF-1 α was detected in 10% of MIBC tumors, showing

heterogeneous expression ranging from 20% to 60% of the tumor area (Figure 6A). HIF-1 α was not found in superficial lesions (Figure 6A). Notably, 59% of studied MIBC were poorly proliferative, including the four hypoxic tumors, whereas only 15% of NMIBC presented a Ki-67^{low} phenotype. Also, HIF-1 α -positive tumor areas did not express Ki-67, in agreement with the acquisition of quiescent phenotypes by hypoxic cells (Figure 6B). However, no associations between the hypoxic phenotype and prognosis were found, as these were already highly aggressive lesions.

We then elected for downstream molecular studies of tumors showing diffuse and intense nuclear HIF-1 α expressions (>50% of the tumor area). These tumors showed increased AMPK phosphorylation and pAMPK/AMPK ratios in comparison to highly proliferative lesions (Figure 6C), consistent with a catabolic state. Subsequent phosphoproteomics highlighted marked differences between hypoxic and non-hypoxic tumors and striking similarities between hypoxic tumors and cell lines in terms of kinase activation (Figures 6D and 6F; Tables S5 and S6). Namely, we found increased PRKCZ and BRAF phosphorylation, contrasting with significantly lower SRC, CDK1, MTOR, CDK2, RPS6KA1, and MAPK3 activation (Figures 6E and 6F). Likewise, altered pathways were also common, with emphasis on endocytosis, cell-cycle arrest, senescence, autophagy, and invasion/cell motility (Figure 6G). Furthermore, hypoxic tumors exhibited elevated expression of hypoxia-associated poor-prognosis markers *TMEM* and *SLC2A3* (Figures 2F and S9). Moreover, 75% of hypoxic tumors co-overexpress at least two out of four hypoxia-linked genes with prognostic significance (Figure 2F), in contrast to 33% under normoxia, underscoring their molecular resemblance to stressed cells *in vitro*.

The glycome of hypoxic tumors was subsequently characterized by mass spectrometry, revealing the sialyl-T antigen as the predominant glycan and lower levels of core 2 O-glycans compared to other shorter glycans (Figure 6H; Table S11), resembling stressed cell lines. The major difference was the absence of core 3 as well as fucosylated T antigens, invariably present in cell models. Trace amounts of STn were also detected

Figure 6. Hypoxic BLCA, characterized by high nuclear HIF-1 α expression and low proliferation, shares malignant molecular features with hypoxic and glucose-deprived cells *in vitro*, including simple glyco-phenotypes

(A and B) Roughly 10% of MIBC tumors display a hypoxic fingerprint (HIF-1 α ^{positive}/Ki-67^{low}) that was not observed in NMIBC and most MIBC tumors (HIF-1 α ^{negative}/Ki-67^{high}), indicating a potential link to aggressiveness.

(C) Hypoxic tumors display significantly higher AMPK phosphorylation compared to proliferative cases, denoting a catabolic state.

(D) Hypoxic tumors show distinct cellular signaling pathway activation compared to proliferative tumors. PCA for phosphoproteomics data indicates that PC1 (58% variance) primarily separates hypoxic from proliferative tumors, whereas PC2 (15% variance) highlights marked differences among hypoxic tumors.

(E) Kinase-Substrate enrichment analysis supports major cell rewiring in hypoxic tumors. Kinases color-coded in red are significantly activated, whereas blue is significantly inactivated.

(F) Hypoxic tumors share common kinase activation patterns with stressed BLCA cells *in vitro*.

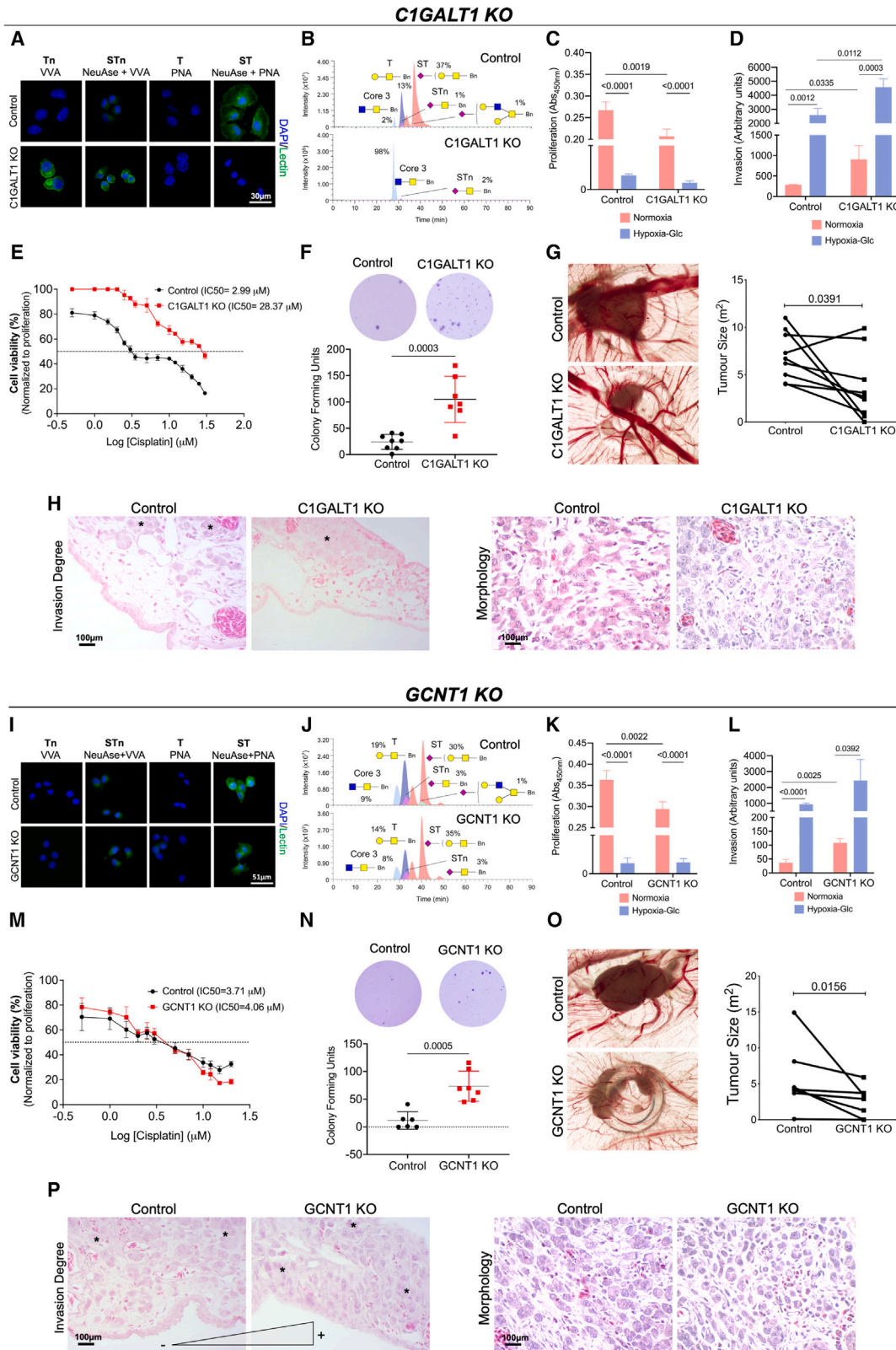
(G) KEGG pathway enrichment analysis indicates significant alterations in cell signaling pathways, promoting cell motility, cellular senescence, and autophagy in hypoxic tumors as found in stressed cells *in vitro*.

(H) Hypoxic tumors present simple O-glyco-phenotypes compared to proliferative tumors. nanoLC-MS/MS reveals more homogeneous O-glycome in hypoxic tumors with scarce core 2 glycans. We represent the most abundant structures also found in cell lines, keeping reference to their original relative abundance in relation to all identified glycan species.

(I) Hypoxic tumors N-glycome is enriched for oligomannose N-glycans, whereas proliferative tumors are enriched for complex N-glycans.

(J and K) Hypoxic tumors show higher levels of Tn and sialylated T antigens and lower levels of sialylated Lewis antigens in O-glycans compared to proliferative tumors, reinforcing the primary suppression of O-glycan extension. NeuAse means sialidase neuraminidase.

(L) In hypoxic tumors, Tn and sialylated T antigens co-localize with high HIF-1 α . Normoxic, proliferative tumors lack HIF-1 α and show low levels of sialylated T antigens and no Tn antigens. Healthy urothelium from non-cancerous individuals served as a negative control for HIF-1 α , low Tn, and sialylated T antigens expression. Unpaired t test and Mann-Whitney test were used for statistical analysis. Results were considered statistically significant when $p < 0.05$.



(legend on next page)

(Table S11). Contrastingly, HIF-1 α ^{negative}/Ki-67^{high} tumors were more heterogeneous, with some tumors showing hypoxic-like glycopatterns, whereas others exhibited a high percentage of core 2 elongations and lower sialyl-T expressions (Figure 6H), suggesting that other factors may also drive altered glycosylation. Semi-quantitative assessment of major glycans linked to hypoxia by lectin immunohistochemistry further reinforced the adoption of a shorter glyco-phenotype by hypoxic tumors (Figures 6J and 6K). Specifically, hypoxic tumors exhibited significantly elevated expressions of Tn and sialyl-T antigens compared to HIF-1 α ^{negative}/Ki-67^{high} tumors (Figures 6J and 6K). Concurrently, these tumors exhibited decreased levels of sialylated Lewis antigens following PNGase F digestion, indicating a loss of O-glycans complexity as observed in hypoxic cell lines *in vitro*. Double immunofluorescence confirmed higher levels of Tn and sialylated T antigens in hypoxic tumor areas (Figure 6L). In addition, we performed a broad characterization of the N-glycome. Despite significant structural diversity, hypoxic tumors were enriched for oligomannose N-glycans (Figure 6I; Table S12), which were not evident *in vitro*. Collectively, these observations highlight fundamental microenvironment-driven molecular grounds shared by cell models and tumors, including the adoption of an immature O-glycocalyx and potentially N-glycosylation, which warrants deeper investigation.

Stress-induced glycome alterations contribute to cancer aggressiveness

T24 cells were glycoengineered (Figures S10 and S11) to display distinct simple O-glycophenotypes and gain more knowledge on the biological role played by altered glycosylation in BLCA. Notably, we also tried to edit 5637 cells without success. We started by overexpressing *ST3GAL1* (Figure S12), which decreased the T antigen and core 1 fucosylation but not core 2-derived glycans, thus not reflecting the hypoxic phenotype (Table S13). Therefore, we glycoengineered cells to hamper O-glycan extension beyond core 1 and core 2 by suppressing *C1GALT1* (Figure S10) and *GCNT1* (Figure S11), respectively, using validated gRNAs⁵⁶ through CRISPR-Cas9 technology. Considering immunoassays using lectins (Figures 7A and S13)

and MS analysis (Figure 7B), we observed a significant increase in Tn antigen levels in *C1GALT1* knockouts. Notably, the reduced diversity of O-glycans, due to the inability to detect the Tn antigen by MS, led to spectra dominated by core 3 structures, despite complementary flow cytometry indicating their mostly residual presence (Figure S13). Interestingly, we also observed marginal expression of STn in these cell lines (Figure S13). Collectively, this demonstrated reduced levels of O-6 GalNAc sialylation and core 3 biosynthesis, despite losing capacity to produce core 1 structures (Figures 7A, 7B, and S13). As a result, we have established a suitable and glyco-homogeneous model for investigating the role of the Tn antigen, which is enriched in stressed cells (Figure 5) as well as hypoxic tumors (Figure 7).

GCNT1 KO cells exhibited a glycome enriched for monosialylated T antigens and a complete absence of core-2-derived glycans (Figures 7I, 7J, and S13; Table S13). Additionally, low levels of core 3 were also observed, whereas Tn and STn levels were low. While presenting a more heterogeneous nature in comparison to *C1GALT1* KO cells, this model provides an opportunity to address the functional role of the ST antigen in a context deprived of more elongated glycans, which constitutes the main structural feature of stressed cells and hypoxic tumors. Interestingly, *ST3GAL1* overexpression on T24 wild-type cells decreased core 1 and fucosyl-core 1, increasing the percentage of sialylated core 2 glycans, whereas for *GCNT1* KO cells it increased T antigen di-sialylation (Table S13). These observations strongly suggest that *ST3GAL1* elevation alone cannot account for the stress-associated glycome.

C1GALT1 and *GCNT1* KO cells, resembling relevant glyco-phenotypic signatures of hypoxic cells, were further used to interrogate the role played by glycosylation in decisive aspects of the disease, namely capacity to proliferate, invade, grow without anchorage, potentially metastasize, and tolerate chemotherapy agents (Figure 7). Both were less proliferative *in vitro* under normoxia as well as hypoxia and low glucose (Figures 7C and 7K). A higher capacity to grow in an anchorage-independent manner and resist anoikis was also observed, supporting increased metastatic potential (Figures 7F and 7N). *C1GALT1* KO cells were more resistant to cisplatin over a wide range of

Figure 7. Hypoxia and low-glucose-induced simple glyco-phenotypes drive relevant cancer-associated hallmarks

(A and B) T24 *C1GALT1* KO cells show complete abrogation of O-glycans extension beyond the Tn antigen, mirroring a major alteration observed in hypoxic tumors. Glycoengineered cells homogeneously express the Tn antigen and show low levels of core 3. Mock controls' glycosylation closely resembles T24 wild-type cells. (C) *C1GALT1* KO cells display reduced proliferation compared to controls under normoxia. Collectively, altered glycosylation impacts proliferation more when compared to hypoxia and glucose deprivation. (D) Under normoxia and hypoxia with glucose deprivation, *C1GALT1* KO glycoengineered cells display significantly enhanced invasion, suggesting a critical role of *C1GALT1* in modulating invasive behavior under stress. (E and F) *C1GALT1* KO cells demonstrate higher resistance to cisplatin (E) and anoikis compared to mock controls (F). (G and H) In CAMs, *C1GALT1* KO cells give rise to smaller tumors (G), in agreement with proliferation studies *in vitro* (C), showing less cohesive features and invasive patterns compared to control (H). (I and J) T24 *GCNT1* KO cells exhibit complete abrogation of O-glycans extension beyond core 1, mirroring another major alteration observed in hypoxic tumors. As a result, glycoengineered cells express high levels of sialylated T antigens, namely sialyl-T, but do not present core 2-derived glycans. Mock controls' glycosylation closely resembles T24 wild-type cells. (K and L) *GCNT1* KO cells display reduced proliferation compared to controls (K) and increased invasion (L) under normoxia, resembling *C1GALT1* KO cells. A higher invasion is also observed under hypoxia-Glc. (M and N) *GCNT1* KO cells demonstrate similar resistance to cisplatin (M) but higher resistance to anoikis compared to mock controls (N). (O and P) In CAMs, *GCNT1* KO cells give rise to smaller (O) and more invasive tumors compared to controls (P). Error bars represent mean \pm SD for three independent experiments. Unpaired t test, two-way ANOVA followed by Tukey's multiple comparison test, and Wilcoxon test were used for statistical analysis. Results were considered statistically significant when $p < 0.05$.

drug concentrations and presented higher IC₅₀ than its control (Figure 7E). Increased invasion was also observed under normoxia and microenvironmental stress (Figure 7D). These findings substantiate a role for the Tn antigen in urothelial cancer cells analogous to the one found for other simple cell models from various solid tumors, such as *C1GALT1* (T-synthase) knockouts^{57,58} and *C1GALT1C1* (COSMC) knockouts.^{59–61} This reinforces the notion of a pan-carcinomic function of Tn antigen driving disease progression. Complementary phosphoproteome characterization confirmed enrichment for pathways consistent with these functional alterations (Figures S14A and S14B), associated to activation of relevant tyrosine kinases also found in hypoxic cells and tumors (Figure S14C), suggesting common molecular grounds supported by immature glycosylation. Interestingly, much less understood *GCNT1* KOs also presented low proliferation and higher invasion capacity in normoxia and hypoxia plus low glucose (Figure 7L) but not increased resistance to cisplatin (Figure 7M). However, the molecular pathways governing glycan-linked functional alterations differ significantly from those in Tn-overexpressing cells (Figures S14D–S14F), thus emphasizing the crucial role of glycosylation in fine-tuning molecular functions.

Finally, we explored the *in ovo* chick chorioallantoic membrane (CAM) assay to assess the biological role of glycans *in vivo*. Notably, T24 CAM models have been previously developed and proven to reflect many histological and molecular features of human bladder tumors,⁶² providing relevant platforms for functional studies. *C1GALT1* and *GCNT1* KO CAM models exhibited significantly smaller tumors when compared to controls, which was consistent with observations *in vitro* (Figures 7G and 7O). Interestingly, despite displaying much smaller lesions, *C1GALT1* KO tumors invaded similarly to controls and exhibited a less cohesive phenotype characterized by a higher number of isolated tumor niches, suggesting higher motility (Figure 7H). *GCNT1* KO models invaded more, reaching the lower allantoic epithelium (endoderm) and, in some cases, even expanding beyond that (Figure 7P). In summary, we have highlighted the different contributions of distinct glycosylation patterns associated with hypoxia and glucose suppression to cancer progression and potentially dissemination. Our findings suggest that the loss of glycan heterogeneity and glycan shortening, regardless of the specific nature of involved glycans, leads to decreased cell proliferation while enhancing invasion, metastasis potential, and resistance to chemotherapy. This suggests a role in promoting hypoxia-related aggressiveness.

DISCUSSION AND CONCLUDING REMARKS

Hypoxia and glucose deprivation are relevant features of solid tumors, arising from sustained proliferative signaling and defective neo-angiogenesis, which decisively shape the molecular and functional phenotypes of tumor cells. The contribution of hypoxia to disease severity, even though extensively studied and rather well known, has been addressed without considering the concomitant influence of low glucose. Acknowledging the complex microenvironmental challenges experienced by cells striving to survive in poorly vascularized tumor areas, the present study is devoted to understanding cells' plasticity and adapt-

ability to these selective pressures, providing the means for more educated and precise interventions. We have comprehensively addressed the impact of microenvironmental stressors (hypoxia and low glucose) at the transcriptome, metabolome, and phosphoproteome levels, which ultimately led us to interrogate the glycome and its biological implications in disease. Strikingly, BLCA models of distinct genetic and molecular backgrounds responded similarly to microenvironmental challenges, denoting common biological grounds facing stress. Cells tolerated low levels of oxygen and glucose, maintaining viability, and avoiding apoptosis, while dramatically decreasing proliferation. Concomitantly, cells became more invasive, denoting an active strategy to escape suboptimal growth conditions. Stress also increased cells' capacity to tolerate the chemotherapy drug cisplatin, possibly explaining the resilient nature of poorly vascularized bladder tumors.^{63,64} Interestingly, this aggressive behavior was completely reverted by re-oxygenation and glucose restoration without compromising cell viability. This further highlighted relevant molecular plasticity accommodating microenvironmental challenges. Under stress, despite the low levels of oxygen, cancer cells adopted mitochondrial fatty acid β -oxidation and oxidative phosphorylation rather than anaerobic glycolysis as the main bioenergetic pathway, explaining the tremendous decrease in lactate production by these cells. Similar observations were made for prostate cancer, where fatty acid oxidation is a dominant bioenergetic pathway rather than glycolysis, showing potential to be the basis of imaging diagnosis and targeted treatment.⁶⁵ To some extent, this also challenges the pivotal role attributed to lactate in the aggressiveness of hypoxic cancer cells in many studies.⁶⁶ We have also found strong indications of mitochondrial autophagy, which has been previously described as a survival mechanism of cancer cells under nutrient deprivation, driving invasion, immune escape, and metastasis.¹¹ Notably, most of the stress-induced molecular alterations found *in vitro* were observed in highly hypoxic and aggressive bladder tumors, providing a basis for patient stratification and targeted interventions.

Finally, we have shown that both stressed BLCA and hypoxic tumors exhibit immature glycophenotypes, characterized by the incapacity to display extended and heterogeneous *O*-glycans. In previous studies, we have linked short glycoforms to advanced stages and poor prognosis,^{16,67–69} without providing a clear rationale for their overexpression in BLCA. Here, we demonstrate that glycocalyx remodeling is an integral component of the adaptive responses of cancer cells to hypoxia and glucose deprivation driving disease aggressiveness. We show that microenvironmental stress induces major metabolic changes that have direct impact on key sugar nucleotides required to support *O*-glycosylation. Namely, we found lower UDP-GalNAc, Neu5Ac, and UDP-Glc, which may ultimately compromise *O*-GalNAc glycosylation initiation, elongation, and capping. Decreased gluconic acid and D-ribulose 5-phosphate as well as AMP, UMP, GMP, and GDP also evidenced alterations in the pentose phosphate pathway required to generate sugar nucleotide precursors of glycosylation. In addition, we found profound disorganization of secretory organelles, which have been previously linked to major alterations in *O*-glycosylation. We have further observed major downregulation of multiple

polypeptide GalNAc-Ts responsible for O-glycosylation initiation, dictating glycosites distribution and density. These events likely contribute to the decreased O-GalNAc glycosylation observed in stressed cells, as well as the reduced structural diversity. Finally, we observed increased expression of ST3Gal-I, which perfectly aligns with the over-sialylation of T antigen observed in stressed cells, ultimately resulting in a premature termination of O-glycans extension. We believe that these events may act synergistically to drive glycolyx remodeling. Changes in protein O-glycosylation may be part of a wide array of responses that make BLCA cells more capable of resisting microenvironmental stress. Specifically, these enabled cells to halt proliferation, resist anoikis, and tolerate chemotherapy. Shorter and more homogeneous O-glycosylation also provides a stress escape mechanism by promoting less cohesive and invasive traits. These observations are in perfect agreement with other reports from simple cell cancer models of different origins, highlighting their pan-carcinomic nature.^{59,60,70} These are seminal findings that offer new insights into understanding the drivers of cancer-associated glycosylation, which have so far been linked to functional mutations in *COSMC*⁷¹ and, more recently, pro-inflammatory immune responses.⁷² Future studies must now focus on conducting an in-depth characterization of the hypoxia-related glycoproteome. This will serve as a starting point for better understanding the molecular mechanisms underlying glycan-triggered aggressiveness, which will be crucial for precise cancer targeting. We also argue that the functional implications arising from stress-induced glycan-remodeling may extend beyond those reported in this study, also serving as a mechanism for evading the immune system. Namely, the Tn antigen found in hypoxic cells is considered a key mechanism of cancer immunosuppression, impairing the maturation of macrophages and dendritic cells by interacting with immune system lectins.⁷³ Investigations on the hypoxia-glycome-immune response axis will likely offer novel insights into the capacity of cells to thrive under stress conditions.

In summary, this study offers a comprehensive exploration of the molecular and functional adaptations undergone by bladder cancer cells when confronted with hypoxia and glucose deprivation, two microenvironmental features that are rarely analyzed together despite their physiological coexistence in tumors. Furthermore, we have addressed a relatively unexplored dimension of molecular adaptation to microenvironmental stress, focusing on glycolyx remodeling and its underlying functional consequences for cancer cells. Our study offers insights into the context of immature glycosylation in BLCA, a factor consistently associated with unfavorable prognosis. It contributes to our understanding of the mechanisms driving BLCA invasion and dissemination, with potential implications for precision therapeutics. Furthermore, it offers seminal observations to better comprehend glycolyx remodeling beyond genetic drivers, underscoring the necessity for a more structured understanding of the physiological dimension of glycosylation.

Limitations of the study

The present study provides an in-depth multi-omics characterization of major cellular molecular rewiring in response to hypoxia and glucose deprivation stressors, emphasizing the impact on

the glycolyx and associating these changes with cancer aggressiveness. However, it does not provide causal connections or molecular clarification of the underlying mechanisms behind how hypoxia and metabolic changes drive glycan alterations toward more aggressive cancer phenotypes. Another key limitation is its sole reliance on *in vitro* cell models to simulate the complex tumor microenvironment, which may not fully capture the heterogeneity and complexity of human tumors, limiting the direct translational potential of the findings.

RESOURCE AVAILABILITY

Lead contact

Further information and requests for resources and reagents should be directed to and will be fulfilled by the lead contact, José Alexandre Ferreira (jose.a.ferreira@ipoporto.min-saude.pt).

Materials availability

All unique models generated in this study are available from the [lead contact](#) with a completed materials transfer agreement.

Data and code availability

- Gene expression data are deposited at Gene Expression Omnibus (GEO) repository (<https://www.ncbi.nlm.nih.gov/geo/>), metabolomics data are deposited at Metabolomics Workbench (<https://www.metabolomicsworkbench.org>), glycomics data are deposited at GlycoPost (<https://glycopost.glycosmos.org/>), and proteomics/phosphoproteomics data are deposited at PRIDE (<https://www.ebi.ac.uk/pride/>). All data are publicly available as of the date of publication. Accession numbers and codes are listed in the [key resources table](#).
- The remaining data and information are available within the main text or [supplemental information](#). Any additional information required to reanalyze the data reported in this paper is available from the [lead contact](#) upon request.
- This paper does not report original code.

ACKNOWLEDGMENTS

The authors wish to acknowledge the Portuguese Foundation for Science and Technology (FCT) for PhD grants SFRH/BD/111242/2015 (A.P.), 2020.09384.BD (D.F.), 2022.12980.BD (A.M.), SFRH/BD/146500/2019 (M.R.S.), 2020.08708.BD (R.F.), SFRH/BD/127327/2016 (C.G.), 2020.09394.BD (S.C.), SFRH/BD/142479/2018 (J.S.), Principal researcher contract 2022.08311.CEECIND (J.A.F.), and junior researcher contacts 2021.03835.CEECIND (A.B.) and 2023.06366.CEECIND (A.P.). FCT is co-financed by European Social Fund under Human Potential Operation Programme from National Strategic Reference Framework. The authors also acknowledge FCT/MCTES funding within the projects RESOLVE (PTDC/MED-OUT/2512/2021) and REVERENT (2022.03621.PTDC; <https://doi.org/10.54499/2022.03621.PTDC>) and funding for the IPO research center (PEst-OE/SAU/UI0776/201, CI-IPOP-29-2016-2022, CI-IPOP-58-2016-2022), CQUM (UID/QUI/00686/2020), and the LAQV research unit (UIDB/50006/2020 | UIDP/50006/2020). We further acknowledge funding for the large-scale proteomics facility, the Netherlands Proteomics Center, through the EU Horizon 2020 program Epic-XS (project 823839). This article is also a result of the project NORTE-01-0145-FEDER-000012 and “The Porto Comprehensive Cancer Center Raquel Seruca” with the reference NORTE-01-0145-FEDER-072678 - Consórcio PORTO.CCC—Porto.Comprehensive Cancer Center Raquel Seruca, supported by NORTE 2020, under the PORTUGAL 2020 Partnership Agreement, through the European Regional Development Fund. This work was also financed by FEDER through the COMPETE 2020 - Operational Programme for Competitiveness and Internationalisation (POCI-01-0145-FEDER-007274 for i3S unit). Finally, the authors also acknowledge the ICBAS PhD Program in Biomedical Sciences and the support of the i3S scientific platforms for the CAM assays and HEMS (PPBI-POCI-01-0145-FEDER-022122). Moreover, the authors

acknowledge the kind collaboration of the pharmaceutical units of IPO-Porto for providing and supervising the handling of clinical-grade cisplatin.

AUTHOR CONTRIBUTIONS

Conceptualization, J.A.F. and A.P.; methodology, A.P., M.R.S., P.P., M.C., A.B., and T.V.; software, A.B., F.T., and T.V.; validation, A.P., D.F., A.M., M.R.S., R.F., T.V., E.F., C.G., and S.C.; investigation, A.P. and D.F.; resources A.M.N.S., A.B., C.P., and A.J.R.H.; data curation, A.P., D.F., A.M., A.B., M.R.S., J.S., L.L., F.T., J.A.F., and A.M.N.S.; writing—original draft, J.A.F. and A.P.; writing—review & editing, A.P., D.F., A.M., M.R.S., R.F., T.V., A.B., E.F., P.P., M.C., C.G., S.C., J.S., L.L., F.T., R.F., C.P., A.J.R.H., M.J.O., A.M.N.S., L.L.S., and J.A.F. Visualization, A.P., A.M., and J.A.F.; supervision, L.L.S., J.A.F., and M.J.O.; project administration, A.P. and J.A.F.; funding acquisition, L.L.S., J.A.F., and A.P.

DECLARATION OF INTERESTS

The authors declare no competing interests.

STAR★METHODS

Detailed methods are provided in the online version of this paper and include the following:

- **KEY RESOURCES TABLE**
- **EXPERIMENTAL MODELS AND STUDY PARTICIPANT DETAILS**
 - Chicken embryos
 - Glycoengineered cell models
 - Patient samples and ethics
- **METHOD DETAILS**
 - HIF-1 α expression
 - Proliferation assay
 - Lactate assay
 - Invasion assay
 - Anchorage-independent growth
 - Cell viability assay
 - Cell cycle analysis
 - Cisplatin resistance
 - Transcriptomics
 - Metabolomics
 - Metabolome and metabolome/transcriptome joint pathway analysis
 - ATP quantification assay
 - Western blot
 - Citrate synthase assay
 - Autophagy assay
 - Transmission electron microscopy
 - Phosphoproteomics and data analysis
 - Glycomics
 - Flow cytometry for glycans detection
 - Immunocytochemistry and immunohistochemistry
 - RT-PCR for glycogenes expression
- **QUANTIFICATION AND STATISTICAL ANALYSIS**
 - Public gene expression and clinical data statistical analysis
 - Statistical analysis

SUPPLEMENTAL INFORMATION

Supplemental information can be found online at <https://doi.org/10.1016/j.isci.2025.111758>.

Received: November 27, 2023

Revised: November 4, 2024

Accepted: January 3, 2025

Published: January 4, 2025

REFERENCES

1. Tan, T.Z., Rouanne, M., Tan, K.T., Huang, R.Y.J., and Thiery, J.P. (2019). Molecular Subtypes of Urothelial Bladder Cancer: Results from a Meta-cohort Analysis of 2411 Tumors. *Eur. Urol.* *75*, 423–432. <https://doi.org/10.1016/j.eururo.2018.08.027>.
2. Petrova, V., Annicchiarico-Petruzzelli, M., Melino, G., and Amelio, I. (2018). The hypoxic tumour microenvironment. *Oncogenesis* *7*, 10. <https://doi.org/10.1038/s41389-017-0011-9>.
3. Jiang, M., Ren, L., Chen, Y., Wang, H., Wu, H., Cheng, S., Li, G., and Yu, S. (2021). Identification of a Hypoxia-Related Signature for Predicting Prognosis and the Immune Microenvironment in Bladder Cancer. *Front. Mol. Biosci.* *8*, 613359. <https://doi.org/10.3389/fmolb.2021.613359>.
4. Liberti, M.V., and Locasale, J.W. (2016). The Warburg Effect: How Does it Benefit Cancer Cells? *Trends Biochem. Sci.* *41*, 211–218. <https://doi.org/10.1016/j.tibs.2015.12.001>.
5. Qiu, Y., Li, P., and Ji, C. (2015). Cell Death Conversion under Hypoxic Condition in Tumor Development and Therapy. *Int. J. Mol. Sci.* *16*, 25536–25551. <https://doi.org/10.3390/ijms161025536>.
6. Luo, Z., Tian, M., Yang, G., Tan, Q., Chen, Y., Li, G., Zhang, Q., Li, Y., Wan, P., and Wu, J. (2022). Hypoxia signaling in human health and diseases: implications and prospects for therapeutics. *Signal Transduct. Targeted Ther.* *7*, 218. <https://doi.org/10.1038/s41392-022-01080-1>.
7. Li, X., Yang, Y., Zhang, B., Lin, X., Fu, X., An, Y., Zou, Y., Wang, J.-X., Wang, Z., and Yu, T. (2022). Lactate metabolism in human health and disease. *Signal Transduct. Targeted Ther.* *7*, 305. <https://doi.org/10.1038/s41392-022-01151-3>.
8. Ferreira, J.A., Peixoto, A., Neves, M., Gaiteiro, C., Reis, C.A., Assaraf, Y.G., and Santos, L.L. (2016). Mechanisms of cisplatin resistance and targeting of cancer stem cells: Adding glycosylation to the equation. *Drug Resist. Updates* *24*, 34–54. <https://doi.org/10.1016/j.drug.2015.11.003>.
9. Stanley, P., Moremen, K.W., Lewis, N.E., Taniguchi, N., and Aebi, M. (2022). N-Glycans. In *Essentials of Glycobiology*, A. Varki, R.D. Cummings, J.D. Esko, P. Stanley, G.W. Hart, M. Aebi, D. Mohnen, T. Kinoshita, N.H. Packer, and J.H. Prestegard, et al., eds., pp. 103–116. <https://doi.org/10.1101/glycobiology.4e.9>.
10. Brockhausen, I., Wandall, H.H., Hagen, K.G.T., and Stanley, P. (2022). O-GalNAc Glycans. In *Essentials of Glycobiology*, A. Varki, R.D. Cummings, J.D. Esko, P. Stanley, G.W. Hart, M. Aebi, D. Mohnen, T. Kinoshita, N.H. Packer, and J.H. Prestegard, et al., eds., pp. 117–128. <https://doi.org/10.1101/glycobiology.4e.10>.
11. Peixoto, A., Relvas-Santos, M., Azevedo, R., Santos, L.L., and Ferreira, J.A. (2019). Protein Glycosylation and Tumor Microenvironment Alterations Driving Cancer Hallmarks. *Front. Oncol.* *9*, 380. <https://doi.org/10.3389/fonc.2019.00380>.
12. Chandler, K.B., Costello, C.E., and Rahimi, N. (2019). Glycosylation in the Tumor Microenvironment: Implications for Tumor Angiogenesis and Metastasis. *Cells* *8*, 544.
13. Pinho, S.S., and Reis, C.A. (2015). Glycosylation in cancer: mechanisms and clinical implications. *Nat. Rev. Cancer* *15*, 540–555. <https://doi.org/10.1038/nrc3982>.
14. Kohnz, R.A., Roberts, L.S., DeTomaso, D., Bideyan, L., Yan, P., Bandyopadhyay, S., Goga, A., Yosef, N., and Nomura, D.K. (2016). Protein Sialylation Regulates a Gene Expression Signature that Promotes Breast Cancer Cell Pathogenicity. *ACS Chem. Biol.* *11*, 2131–2139. <https://doi.org/10.1021/acscchembio.6b00433>.
15. Ying, H., Kimmelman, A.C., Lyssiotis, C.A., Hua, S., Chu, G.C., Fletcher-Sanankone, E., Locasale, J.W., Son, J., Zhang, H., Coloff, J.L., et al. (2012). Oncogenic Kras maintains pancreatic tumors through regulation of anabolic glucose metabolism. *Cell* *149*, 656–670. <https://doi.org/10.1016/j.cell.2012.01.058>.
16. Peixoto, A., Fernandes, E., Gaiteiro, C., Lima, L., Azevedo, R., Soares, J., Cotton, S., Parreira, B., Neves, M., Amaro, T., et al. (2016). Hypoxia

- enhances the malignant nature of bladder cancer cells and concomitantly antagonizes protein O-glycosylation extension. *Oncotarget* 7, 63138–63157. <https://doi.org/10.18632/oncotarget.11257>.
17. Malhotra, R., Tyson, D.G.W., Sone, H., Aoki, K., Kumagai, A.K., and Brosius, F.C., 3rd. (2002). Glucose uptake and adenoviral mediated GLUT1 infection decrease hypoxia-induced HIF-1 α levels in cardiac myocytes. *J. Mol. Cell. Cardiol.* 34, 1063–1073. <https://doi.org/10.1006/jmcc.2002.2047>.
 18. Habuka, M., Fagerberg, L., Hallström, B.M., Pontén, F., Yamamoto, T., and Uhlen, M. (2015). The Urinary Bladder Transcriptome and Proteome Defined by Transcriptomics and Antibody-Based Profiling. *PLoS One* 10, e0145301. <https://doi.org/10.1371/journal.pone.0145301>.
 19. Kojima, E., Takeuchi, A., Haneda, M., Yagi, A., Hasegawa, T., Yamaki, K.I., Takeda, K., Akira, S., Shimokata, K., and Isobe, K.I. (2003). The function of GADD34 is a recovery from a shutoff of protein synthesis induced by ER stress: elucidation by GADD34-deficient mice. *Faseb. J.* 17, 1573–1575. <https://doi.org/10.1096/fj.02-1184fj>.
 20. Ito, S., Tanaka, Y., Oshino, R., Aiba, K., Thanasegaran, S., Nishio, N., and Isobe, K. (2015). GADD34 inhibits activation-induced apoptosis of macrophages through enhancement of autophagy. *Sci. Rep.* 5, 8327. <https://doi.org/10.1038/srep08327>.
 21. Shoshani, T., Faerman, A., Mett, I., Zelin, E., Tenne, T., Gorodin, S., Moshel, Y., Elbaz, S., Budanov, A., Chajut, A., et al. (2002). Identification of a Novel Hypoxia-Inducible Factor 1-Responsive Gene, RTP801, Involved in Apoptosis. *Mol. Cell Biol.* 22, 2283–2293. <https://doi.org/10.1128/MCB.22.7.2283-2293.2002>.
 22. Yalcin, A., Clem, B.F., Imbert-Fernandez, Y., Ozcan, S.C., Peker, S., O'Neal, J., Klarer, A.C., Clem, A.L., Telang, S., and Chesney, J. (2014). 6-Phosphofructo-2-kinase (PFKFB3) promotes cell cycle progression and suppresses apoptosis via Cdk1-mediated phosphorylation of p27. *Cell Death Dis.* 5, e1337. <https://doi.org/10.1038/cddis.2014.292>.
 23. Jung, C.H., Ro, S.H., Cao, J., Otto, N.M., and Kim, D.H. (2010). mTOR regulation of autophagy. *FEBS Lett.* 584, 1287–1295. <https://doi.org/10.1016/j.febslet.2010.01.017>.
 24. Yang, Z., Goronzy, J.J., and Weyand, C.M. (2014). The glycolytic enzyme PFKFB3/phosphofructokinase regulates autophagy. *Autophagy* 10, 382–383. <https://doi.org/10.4161/auto.27345>.
 25. Roberts, D.J., Tan-Sah, V.P., Ding, E.Y., Smith, J.M., and Miyamoto, S. (2014). Hexokinase-II positively regulates glucose starvation-induced autophagy through TORC1 inhibition. *Mol. Cell* 53, 521–533. <https://doi.org/10.1016/j.molcel.2013.12.019>.
 26. Gambardella, G., Staiano, L., Moretti, M.N., De Cegli, R., Fagnocchi, L., Di Tullio, G., Polletti, S., Braccia, C., Armirotti, A., Zippo, A., et al. (2020). GADD34 is a modulator of autophagy during starvation. *Sci. Adv.* 6, eabb0205. <https://doi.org/10.1126/sciadv.abb0205>.
 27. Foltyn, M., Luger, A.-L., Lorenz, N.I., Sauer, B., Mittelbronn, M., Harter, P.N., Steinbach, J.P., and Ronellenfitsch, M.W. (2019). The physiological mTOR complex 1 inhibitor DDIT4 mediates therapy resistance in glioblastoma. *Br. J. Cancer* 120, 481–487. <https://doi.org/10.1038/s41416-018-0368-3>.
 28. Li, H., Wang, X., Tang, J., Zhao, H., and Duan, M. (2019). Decreased expression levels of ELOVL6 indicate poor prognosis in hepatocellular carcinoma. *Oncol. Lett.* 18, 6214–6220. <https://doi.org/10.3892/ol.2019.10974>.
 29. Karagiannidis, I., Jerman, S.J., Jacenik, D., Phinney, B.B., Yao, R., Prossnitz, E.R., and Beswick, E.J. (2020). G-CSF and G-CSFR Modulate CD4 and CD8 T Cell Responses to Promote Colon Tumor Growth and Are Potential Therapeutic Targets. *Front. Immunol.* 11, 1885. <https://doi.org/10.3389/fimmu.2020.01885>.
 30. Milde-Langosch, K., Kappes, H., Riethdorf, S., Löning, T., and Bamberg, A.M. (2003). FosB is highly expressed in normal mammary epithelia, but down-regulated in poorly differentiated breast carcinomas. *Breast Cancer Res. Treat.* 77, 265–275. <https://doi.org/10.1023/a:1021887100216>.
 31. Tang, C., Jiang, Y., Shao, W., Shi, W., Gao, X., Qin, W., Jiang, T., Wang, F., and Feng, S. (2016). Abnormal expression of FOSB correlates with tumor progression and poor survival in patients with gastric cancer. *Int. J. Oncol.* 49, 1489–1496. <https://doi.org/10.3892/ijo.2016.3661>.
 32. Baron, V., Adamson, E.D., Calogero, A., Ragona, G., and Mercola, D. (2006). The transcription factor Egr1 is a direct regulator of multiple tumor suppressors including TGF β 1, PTEN, p53, and fibronectin. *Cancer Gene Ther.* 13, 115–124. <https://doi.org/10.1038/sj.cgt.7700896>.
 33. Plotnik, J.P., Budka, J.A., Ferris, M.W., and Hollenhorst, P.C. (2014). ETS1 is a genome-wide effector of RAS/ERK signaling in epithelial cells. *Nucleic Acids Res.* 42, 11928–11940. <https://doi.org/10.1093/nar/gku929>.
 34. Chang, B., Meng, J., Zhu, H., Du, X., Sun, L., Wang, L., Li, S., and Yang, G. (2018). Overexpression of the recently identified oncogene REDD1 correlates with tumor progression and is an independent unfavorable prognostic factor for ovarian carcinoma. *Diagn. Pathol.* 13, 87. <https://doi.org/10.1186/s13000-018-0754-4>.
 35. Tsui, K.H., Lin, Y.H., Chang, K.S., Hou, C.P., Chen, P.J., Feng, T.H., and Juang, H.H. (2019). Transgelin, a p53 and PTEN-Upregulated Gene, Inhibits the Cell Proliferation and Invasion of Human Bladder Carcinoma Cells *In Vitro* and *In Vivo*. *Int. J. Mol. Sci.* 20, 4946. <https://doi.org/10.3390/ijms20194946>.
 36. Li, J., Wang, X., Chen, L., Zhang, J., Zhang, Y., Ren, X., Sun, J., Fan, X., Fan, J., Li, T., et al. (2022). TMEM158 promotes the proliferation and migration of glioma cells via STAT3 signaling in glioblastomas. *Cancer Gene Ther.* 29, 1117–1129. <https://doi.org/10.1038/s41417-021-00414-5>.
 37. Jin, X., Yun, S.J., Jeong, P., Kim, I.Y., Kim, W.J., and Park, S. (2014). Diagnosis of bladder cancer and prediction of survival by urinary metabolomics. *Oncotarget* 5, 1635–1645. <https://doi.org/10.18632/oncotarget.1744>.
 38. Rodrigues, D., Jerónimo, C., Henrique, R., Belo, L., de Lourdes Bastos, M., de Pinho, P.G., and Carvalho, M. (2016). Biomarkers in bladder cancer: A metabolomic approach using *in vitro* and *ex vivo* model systems. *Int. J. Cancer* 139, 256–268. <https://doi.org/10.1002/ijc.30016>.
 39. Koundouros, N., and Poulogiannis, G. (2020). Reprogramming of fatty acid metabolism in cancer. *Br. J. Cancer* 122, 4–22. <https://doi.org/10.1038/s41416-019-0650-z>.
 40. Icard, P., and Lincet, H. (2016). The reduced concentration of citrate in cancer cells: An indicator of cancer aggressiveness and a possible therapeutic target. *Drug Resist. Updates* 29, 47–53. <https://doi.org/10.1016/j.drug.2016.09.003>.
 41. Al-Maghrabi, J., Qureshi, I.A., Butt, N.S., and Khabaz, M.N. (2018). Phosphorylated AMP-activated protein kinase expression is significantly associated with poor clinical outcomes in bladder carcinoma patients. *Int. J. Clin. Exp. Pathol.* 11, 3718–3725.
 42. Rao, S., Oyang, L., Liang, J., Yi, P., Han, Y., Luo, X., Xia, L., Lin, J., Tan, S., Hu, J., et al. (2021). Biological Function of HYOU1 in Tumors and Other Diseases. *OncoTargets Ther.* 14, 1727–1735. <https://doi.org/10.2147/ott.S297332>.
 43. Varone, E., Decio, A., Chemorudskiy, A., Minoli, L., Brunelli, L., Ioli, F., Piotti, A., Pastorelli, R., Fratelli, M., Gobbi, M., et al. (2021). The ER stress response mediator ERO1 triggers cancer metastasis by favoring the angiogenic switch in hypoxic conditions. *Oncogene* 40, 1721–1736. <https://doi.org/10.1038/s41388-021-01659-y>.
 44. Wen, Y.D., Zhu, X.S., Li, D.J., Zhao, Q., Cheng, Q., and Peng, Y. (2021). Proteomics-based prognostic signature and nomogram construction of hypoxia microenvironment on deteriorating glioblastoma (GBM) pathogenesis. *Sci. Rep.* 11, 17170. <https://doi.org/10.1038/s41598-021-95980-x>.
 45. Zhu, T., Su, Q., Wang, C., Shen, L., Chen, H., Feng, S., Peng, X., Chen, S., Wang, Y., Jiang, H., and Chen, J. (2021). SDF4 Is a Prognostic Factor for 28-Days Mortality in Patients With Sepsis via Negatively Regulating ER Stress. *Front. Immunol.* 12, 659193. <https://doi.org/10.3389/fimmu.2021.659193>.

46. Wang, Y., and Wan, Y.J.Y. (2020). Golgi protein 73, hepatocellular carcinoma and other types of cancers. *Liver Res.* 4, 161–167. <https://doi.org/10.1016/j.livres.2020.09.003>.
47. Della Peruta, M., Giagulli, C., Laudanna, C., Scarpa, A., and Sorio, C. (2010). RHOA and PRKCZ control different aspects of cell motility in pancreatic cancer metastatic clones. *Mol. Cancer* 9, 61. <https://doi.org/10.1186/1476-4598-9-61>.
48. Black, A.R., and Black, J.D. (2012). Protein kinase C signaling and cell cycle regulation. *Front. Immunol.* 3, 423. <https://doi.org/10.3389/fimmu.2012.00423>.
49. Bui, N.-L.-C., Pandey, V., Zhu, T., Ma, L., Basappa, and Lobie, P.E. (2018). Bad phosphorylation as a target of inhibition in oncology. *Cancer Lett.* 415, 177–186. <https://doi.org/10.1016/j.canlet.2017.11.017>.
50. Korotchkina, L.G., and Patel, M.S. (1995). Mutagenesis studies of the phosphorylation sites of recombinant human pyruvate dehydrogenase. Site-specific regulation. *J. Biol. Chem.* 270, 14297–14304. <https://doi.org/10.1074/jbc.270.24.14297>.
51. Herzig, S., and Shaw, R.J. (2018). AMPK: guardian of metabolism and mitochondrial homeostasis. *Nat. Rev. Mol. Cell Biol.* 19, 121–135. <https://doi.org/10.1038/nrm.2017.95>.
52. Yi, Y.W., You, K.S., Park, J.S., Lee, S.G., and Seong, Y.S. (2021). Ribosomal Protein S6: A Potential Therapeutic Target against Cancer? *Int. J. Mol. Sci.* 23, 48. <https://doi.org/10.3390/ijms23010048>.
53. Leicht, D.T., Balan, V., Kaplun, A., Singh-Gupta, V., Kaplun, L., Dobson, M., and Tzivion, G. (2007). Raf kinases: function, regulation and role in human cancer. *Biochim. Biophys. Acta* 1773, 1196–1212. <https://doi.org/10.1016/j.bbamcr.2007.05.001>.
54. Rutkovsky, A.C., Yeh, E.S., Guest, S.T., Findlay, V.J., Muise-Helmericks, R.C., Armeson, K., and Ethier, S.P. (2019). Eukaryotic initiation factor 4E-binding protein as an oncogene in breast cancer. *BMC Cancer* 19, 491. <https://doi.org/10.1186/s12885-019-5667-4>.
55. Cai, H., Zheng, D., Yao, Y., Yang, L., Huang, X., and Wang, L. (2022). Roles of Embryonic Lethal Abnormal Vision-Like RNA Binding Proteins in Cancer and Beyond. *Front. Cell Dev. Biol.* 10, 847761. <https://doi.org/10.3389/fcell.2022.847761>.
56. Narimatsu, Y., Joshi, H.J., Yang, Z., Gomes, C., Chen, Y.H., Lorenzetti, F.C., Furukawa, S., Schjoldager, K.T., Hansen, L., Clausen, H., et al. (2018). A validated gRNA library for CRISPR/Cas9 targeting of the human glycosyltransferase genome. *Glycobiology* 28, 295–305. <https://doi.org/10.1093/glycob/cwx101>.
57. Lee, P.-C., Chen, S.-T., Kuo, T.-C., Lin, T.-C., Lin, M.-C., Huang, J., Hung, J.-S., Hsu, C.-L., Juan, H.-F., Lee, P.-H., and Huang, M.-C. (2020). C1GALT1 is associated with poor survival and promotes soluble Ephrin A1-mediated cell migration through activation of EPHA2 in gastric cancer. *Oncogene* 39, 2724–2740. <https://doi.org/10.1038/s41388-020-1178-7>.
58. Chugh, S., Barkeer, S., Rachagani, S., Nimmakayala, R.K., Perumal, N., Pothuraju, R., Atri, P., Mahapatra, S., Thapa, I., Talmon, G.A., et al. (2018). Disruption of C1galt1 Gene Promotes Development and Metastasis of Pancreatic Adenocarcinomas in Mice. *Gastroenterology* 155, 1608–1624. <https://doi.org/10.1053/j.gastro.2018.08.007>.
59. Radhakrishnan, P., Dabelsteen, S., Madsen, F.B., Francavilla, C., Kopp, K.L., Steentoft, C., Vakhrushev, S.Y., Olsen, J.V., Hansen, L., Bennett, E.P., et al. (2014). Immature truncated O-glycophenotype of cancer directly induces oncogenic features. *Proc. Natl. Acad. Sci. USA* 111, E4066–E4075. <https://doi.org/10.1073/pnas.1406619111>.
60. Freitas, D., Campos, D., Gomes, J., Pinto, F., Macedo, J.A., Matos, R., Mereiter, S., Pinto, M.T., Polónia, A., Gartner, F., et al. (2019). O-glycans truncation modulates gastric cancer cell signaling and transcription leading to a more aggressive phenotype. *EBioMedicine* 40, 349–362. <https://doi.org/10.1016/j.ebiom.2019.01.017>.
61. Hofmann, B.T., Schlüter, L., Lange, P., Mercanoglu, B., Ewald, F., Fölster, A., Picksak, A.S., Harder, S., El Gammal, A.T., Grupp, K., et al. (2015). COSMC knockdown mediated aberrant O-glycosylation promotes oncogenic properties in pancreatic cancer. *Mol. Cancer* 14, 109. <https://doi.org/10.1186/s12943-015-0386-1>.
62. Hu, J., Ishihara, M., Chin, A.I., and Wu, L. (2019). Establishment of xenografts of urological cancers on chicken chorioallantoic membrane (CAM) to study metastasis. *Precis. Clin. Med.* 2, 140–151. <https://doi.org/10.1093/pcmedi/pbz018>.
63. Koukourakis, M.I., Kakouratos, C., Kalamida, D., Bampali, Z., Mavropoulou, S., Sivridis, E., and Giatromanolaki, A. (2016). Hypoxia-inducible proteins HIF1 α and lactate dehydrogenase LDH5, key markers of anaerobic metabolism, relate with stem cell markers and poor post-radiotherapy outcome in bladder cancer. *Int. J. Radiat. Biol.* 92, 353–363. <https://doi.org/10.3109/09553002.2016.1162921>.
64. Afonso, J., Santos, L.L., Longatto-Filho, A., and Baltazar, F. (2020). Competitive glucose metabolism as a target to boost bladder cancer immunotherapy. *Nat. Rev. Urol.* 17, 77–106. <https://doi.org/10.1038/s41585-019-0263-6>.
65. Liu, Y. (2006). Fatty acid oxidation is a dominant bioenergetic pathway in prostate cancer. *Prostate Cancer Prostatic Dis.* 9, 230–234. <https://doi.org/10.1038/sj.pcan.4500879>.
66. DeBerardinis, R.J., and Chandel, N.S. (2020). We need to talk about the Warburg effect. *Nat. Metab.* 2, 127–129. <https://doi.org/10.1038/s42255-020-0172-2>.
67. Costa, C., Pereira, S., Lima, L., Peixoto, A., Fernandes, E., Neves, D., Neves, M., Gaiteiro, C., Tavares, A., Gil da Costa, R.M., et al. (2015). Abnormal Protein Glycosylation and Activated PI3K/Akt/mTOR Pathway: Role in Bladder Cancer Prognosis and Targeted Therapeutics. *PLoS One* 10, e0141253. <https://doi.org/10.1371/journal.pone.0141253>.
68. Cotton, S., Azevedo, R., Gaiteiro, C., Ferreira, D., Lima, L., Peixoto, A., Fernandes, E., Neves, M., Neves, D., Amaro, T., et al. (2017). Targeted O-glycoproteomics explored increased sialylation and identified MUC16 as a poor prognosis biomarker in advanced-stage bladder tumours. *Mol. Oncol.* 11, 895–912. <https://doi.org/10.1002/1878-0261.12035>.
69. Ferreira, J.A., Videira, P.A., Lima, L., Pereira, S., Silva, M., Carrascal, M., Severino, P.F., Fernandes, E., Almeida, A., Costa, C., et al. (2013). Overexpression of tumour-associated carbohydrate antigen sialyl-Tn in advanced bladder tumours. *Mol. Oncol.* 7, 719–731. <https://doi.org/10.1016/j.molonc.2013.03.001>.
70. Coelho, R., Marcos-Silva, L., Mendes, N., Pereira, D., Brito, C., Jacob, F., Steentoft, C., Mandel, U., Clausen, H., David, L., and Ricardo, S. (2018). Mucins and Truncated O-Glycans Unveil Phenotypic Discrepancies between Serous Ovarian Cancer Cell Lines and Primary Tumours. *Int. J. Mol. Sci.* 19, 2045. <https://doi.org/10.3390/ijms19072045>.
71. Wang, Y., Ju, T., Ding, X., Xia, B., Wang, W., Xia, L., He, M., and Cummings, R.D. (2010). Cosmc is an essential chaperone for correct protein O-glycosylation. *Proc. Natl. Acad. Sci. USA* 107, 9228–9233. <https://doi.org/10.1073/pnas.0914004107>.
72. Dewald, J.H., Colomb, F., Bobowski-Gerard, M., Groux-Degroote, S., and Delannoy, P. (2016). Role of Cytokine-Induced Glycosylation Changes in Regulating Cell Interactions and Cell Signaling in Inflammatory Diseases and Cancer. *Cells* 5, 43. <https://doi.org/10.3390/cells5040043>.
73. Peixoto, A., Miranda, A., Santos, L.L., and Ferreira, J.A. (2022). A roadmap for translational cancer glycoimmunology at single cell resolution. *J. Exp. Clin. Cancer Res.* 41, 143. <https://doi.org/10.1186/s13046-022-02335-z>.
74. Písal, R.V., Hřebíková, H., Chvátalová, J., Kunke, D., Filip, S., and Mokry, J. (2016). Detection of Mycoplasma Contamination Directly from Culture Supernatant Using Polymerase Chain Reaction. *Folia Biol.* 62, 203–206.
75. Song, J., Miermont, A., Lim, C.T., and Kamm, R.D. (2018). A 3D microvascular network model to study the impact of hypoxia on the extravasation potential of breast cell lines. *Sci. Rep.* 8, 17949. <https://doi.org/10.1038/s41598-018-36381-5>.
76. Candolfi, M., Curtin, J.F., Yagiz, K., Assi, H., Wibowo, M.K., Alzadeh, G.E., Foulad, D., Muhammad, A.K.M.G., Salehi, S., Keech, N., et al. (2011). B cells are critical to T-cell-mediated antitumor immunity induced by a

- combined immune-stimulatory/conditionally cytotoxic therapy for glioblastoma. *Neoplasia* 13, 947–960. <https://doi.org/10.1593/neo.11024>.
77. Lambert, C.M., Roy, M., Robitaille, G.A., Richard, D.E., and Bonnet, S. (2010). HIF-1 inhibition decreases systemic vascular remodelling diseases by promoting apoptosis through a hexokinase 2-dependent mechanism. *Cardiovasc. Res.* 88, 196–204. <https://doi.org/10.1093/cvr/cvq152>.
78. Borowicz, S., Van Scoyk, M., Avasarala, S., Karuppusamy Rathinam, M.K., Tauler, J., Bikkavilli, R.K., and Winn, R.A. (2014). The soft agar colony formation assay. *J. Vis. Exp.* 92, e51998. <https://doi.org/10.3791/51998>.
79. Strober, W. (2001). Trypan blue exclusion test of cell viability. *Curr. Protoc. Immunol. Appendix 3*, Appendix 3B. <https://doi.org/10.1002/0471142735.ima03bs21>.
80. Peixoto, A., Ferreira, D., Azevedo, R., Freitas, R., Fernandes, E., Relvas-Santos, M., Gaiteiro, C., Soares, J., Cotton, S., Teixeira, B., et al. (2021). Glycoproteomics identifies HOMER3 as a potentially targetable biomarker triggered by hypoxia and glucose deprivation in bladder cancer. *J. Exp. Clin. Cancer Res.* 40, 191. <https://doi.org/10.1186/s13046-021-01988-6>.
81. Coore, H.G., Denton, R.M., Martin, B.R., and Randle, P.J. (1971). Regulation of adipose tissue pyruvate dehydrogenase by insulin and other hormones. *Biochem. J.* 125, 115–127. <https://doi.org/10.1042/bj1250115>.
82. Veth, T.S., Francavilla, C., Heck, A.J.R., and Altelaar, M. (2023). Elucidating Fibroblast Growth Factor-Induced Kinome Dynamics Using Targeted Mass Spectrometry and Dynamic Modeling. *Mol. Cell. Proteomics* 22, 100594. <https://doi.org/10.1016/j.mcpro.2023.100594>.
83. Tyanova, S., Temu, T., and Cox, J. (2016). The MaxQuant computational platform for mass spectrometry-based shotgun proteomics. *Nat. Protoc.* 11, 2301–2319. <https://doi.org/10.1038/nprot.2016.136>.
84. Leeming, M.G., O'Callaghan, S., Licata, L., Iannuccelli, M., Lo Surdo, P., Micarelli, E., Ang, C.S., Nie, S., Varshney, S., Ameen, S., et al. (2021). Phosphomatics: interactive interrogation of substrate-kinase networks in global phosphoproteomics datasets. *Bioinformatics* 37, 1635–1636. <https://doi.org/10.1093/bioinformatics/btaa916>.
85. Kudelka, M.R., Antonopoulos, A., Wang, Y., Duong, D.M., Song, X., Seyfried, N.T., Dell, A., Haslam, S.M., Cummings, R.D., and Ju, T. (2016). Cellular O-Glycome Reporter/Amplification to explore O-glycans of living cells. *Nat. Methods* 13, 81–86. <https://doi.org/10.1038/nmeth.3675>.
86. Fernandes, E., Freitas, R., Ferreira, D., Soares, J., Azevedo, R., Gaiteiro, C., Peixoto, A., Oliveira, S., Cotton, S., Relvas-Santos, M., et al. (2020). Nucleolin-Sle A Glycoforms as E-Selectin Ligands and Potentially Targetable Biomarkers at the Cell Surface of Gastric Cancer Cells. *Cancers* 12, 861. <https://doi.org/10.3390/cancers12040861>.
87. Zhang, T., Madunić, K., Holst, S., Zhang, J., Jin, C., Ten Dijke, P., Karlsson, N.G., Stavenhagen, K., and Wuhrer, M. (2020). Development of a 96-well plate sample preparation method for integrated N- and O-glycomics using porous graphitized carbon liquid chromatography-mass spectrometry. *Mol. Omics* 16, 355–363. <https://doi.org/10.1039/c9mo00180h>.
88. Chen, H.Z., Guo, S., Li, Z.Z., Lu, Y., Jiang, D.S., Zhang, R., Lei, H., Gao, L., Zhang, X., Zhang, Y., et al. (2014). A critical role for interferon regulatory factor 9 in cerebral ischemic stroke. *J. Neurosci.* 34, 11897–11912. <https://doi.org/10.1523/jneurosci.1545-14.2014>.
89. Lima, L., Gaiteiro, C., Peixoto, A., Soares, J., Neves, M., Santos, L.L., and Ferreira, J.A. (2016). Reference Genes for Addressing Gene Expression of Bladder Cancer Cell Models under Hypoxia: A Step Towards Transcriptionomic Studies. *PLoS One* 11, e0166120. <https://doi.org/10.1371/journal.pone.0166120>.

STAR★METHODS

KEY RESOURCES TABLE

REAGENT or RESOURCE	SOURCE	IDENTIFIER
Antibodies		
Anti-AMPK alpha 1 + AMPK alpha 2 antibody [34.2]	Abcam	ab80039
Anti-B3GNT6 polyclonal antibody	Invitrogen	PA5-90159
Anti-C1GALT1 antibody	Novus Biologicals	NBP1-88477
Anti-C1GALT1C1 antibody	Sigma-Aldrich	HPA015632
Anti-GCNT1 antibody	Abcam	ab102665
Anti-ST3Gal I antibody	Abcam	ab96129
Goat anti-Rabbit IgG (H+L) Cross-Adsorbed Secondary Antibody, Alexa Fluor™ 594	Thermo Fisher Scientific	A-11012
Goat anti-Rabbit IgG (H+L) Secondary Antibody, HRP	Invitrogen	65-6120
Goat anti-Rabbit IgG (H+L) Secondary Antibody, HRP	Thermo Fisher Scientific	31460
Monoclonal Mouse Anti-Human Ki-67 [MIB-1]	Agilent	M724029-2
Mouse IgG1 [MOPC-21] isotype control	Abcam	ab18443
Mouse monoclonal [CA19-9-203] to CA19-9	Abcam	ab116024
Mouse monoclonal anti-tag-72 antibody [B72.3 + CC49]	Abcam	ab199002
Peroxidase AffiniPure Goat anti-Mouse IgG (H+L)	Jackson ImmunoResearch	115-035-003
Polyclonal rabbit anti-mouse immunoglobulins/FITC	DAKO	F0313
Purified anti-human Sialyl Lewis X (dimeric), clone FH6	BioLegend	368102
Rabbit monoclonal [EP1215Y] to HIF-1 alpha	Abcam	ab51608
Rabbit polyclonal to AMPK alpha 1 (phospho T183) + AMPK alpha 2 (phospho T172)	Abcam	ab23875
Chemicals, peptides, and recombinant proteins		
0.05% Trypsin-EDTA	Gibco	25300-062
4',6-Diamidino-2-phenylindole dihydrochloride	Thermo Fisher Scientific	62247
5,5'-dithiobis-(2-nitrobenzoic acid)	Sigma-Aldrich	69-78-3
Accutase - Enzyme Cell Detachment Medium	ThermoFisher Scientific	00-4555-56
Acetic acid	Sigma-Aldrich	A6283
Acetonitrile	Merk	14261-2L
Acetyl coenzyme A trisodium salt	Sigma-Aldrich	A2056
Ammonium acetate, BioXtra, ≥98%	Sigma-Aldrich	A7330
Antigen Unmasking Solution, Citrate-Based	Vector Laboratories	H-3300-250
Cisplatin 1mg/ml concentrate solution for infusion	Accord Healthcare, S.L.U	
Crystal Violet	Sigma-Aldrich	61135
Deferoxamine mesylate salt	Sigma-Aldrich	D9533
Dimethyl sulfoxide	Sigma-Aldrich	D26650
DL-Dithiothreitol	Sigma-Aldrich	D9779
Formaldehyde/Glutaraldehyde 2.5% in Sodium Cacodylate Buffer, 7.4 pH 10 ML	Electron Microscopy Sciences	15949
Formalin solution, neutral buffered, 10%	Sigma-Aldrich	HT50128
Formic acid	Merk	5.33002.0050
GeneArt™ Platinum Cas9 Nuclease	Thermo Fisher Scientific	B25640
Glycerol for molecular biology, ≥99.0%	Sigma-Aldrich	G5516
Guanidine hydrochloride	Sigma-Aldrich	G4505
Halt™ Protease and Phosphatase Inhibitor Cocktail	Thermo Fisher Scientific	78440

(Continued on next page)

Continued

REAGENT or RESOURCE	SOURCE	IDENTIFIER
Hydrochloric acid, 36.5-38.0%, BioReagent, for molecular biology	Sigma-Aldrich	H1758
jetPRIME® transfection reagent	PolyPlus Transfection	114-01
Lead citrate	Electron Microscopy Sciences	22410
Magnesium chloride anhydrous	Sigma-Aldrich	M8266
Methanol	Merck	34860-1L-R
MTT (3-(4,5-Dimethylthiazol-2-yl)-2,5-Diphenyltetrazolium Bromide)	ThermoFisher Scientific	M6494
Neuraminidase from <i>Clostridium perfringens</i>	Sigma-Aldrich	N5631
NONIDET™ P 40 Substitute Bioextra, mix	Sigma-Aldrich	74385
Osmium tetroxide	Electron Microscopy Sciences	20816-12-0
Oxaloacetic acid	Sigma-Aldrich	328-42-7
Paraformaldehyde	Sigma-Aldrich	158127
PNGase F Glycosidase from <i>Elizabethkingia miricola</i>	Promega	PROMV4831
Ponceau S anionic dye	Sigma-Aldrich	P3504
Potassium hydroxide	Sigma-Aldrich	306568
Puromycin, Dihydrochloride	EMD Millipore	540222
SeaPlaque® Agarose	Lonza	50101
Sodium borohydride	Honeywell Fluka™	7132
Sodium chloride	Sigma-Aldrich	7647-14-5
Triton™-X	Sigma-Aldrich	T8787
Trizma® base	Sigma-Aldrich	T6066
Trypan Blue Stain (0.4%)	Gibco	15250-061
UAR-EMS Uranyl Acetate Replacement Stain	Electron Microscopy Science	22405
Biotinylated Peanut Agglutinin (PNA)	Vector Laboratories	B-1075-5
Biotinylated Vicia Villosa Lectin (VVA)	Vector Laboratories	B-1235
Griffonia (Bandeiraea) Simplicifolia Lectin II (GSL II, BSL II), Fluorescein	Vector Laboratories	FL-1211-2
Peanut Agglutinin (PNA), Fluorescein	Vector Laboratories	FL-1071
Vicia Villosa Lectin (VVL, VVA), Fluorescein	Vector Laboratories	FL-1231-2
Critical commercial assays		
Autophagy Assay Kit	Sigma-Aldrich	MAK138
Cell Proliferation ELISA, BrdU	Roche	11647229001
Dead Cell Apoptosis Kits with Annexin V for Flow Cytometry	ThermoFisher Scientific	V13242
Fluorometric ATP assay kit	Abcam	ab83355
HIF-1 Alpha ELISA Kit	Invitrogen™	EHIF1A
L-Lactate Assay Kit	Abcam	ab65331
RNeasy Plus Mini Kit	Qiagen	74134
TAAB 812 (Epon) Premix Kit Medium	TAAB	T031
Deposited data		
Glycomics data	[Database]: GlycoPost (https://glycopost.glycosmos.org/)	GPST000517.0
Metabolomics data	[Database]: Metabolomics Workbench (https://www.metabolomicsworkbench.org)	ST003639
Phosphoproteomics data	[Database]: PRIDE (https://www.ebi.ac.uk/pride/)	PXD045777
Transcriptomics data	[Database]: GEO (https://www.ncbi.nlm.nih.gov/geo/)	GSE284635
Experimental models: Cell lines		
Human BLCA cell line 5637 (white male patient)	ATCC	HTB-9™
Human BLCA cell line HT1197 (white male patient)	ATCC	CRL-1473™

(Continued on next page)

Continued

REAGENT or RESOURCE	SOURCE	IDENTIFIER
Human BLCA cell line RT4 (white male patient)	ATCC	HTB-2 TM
Human BLCA cell line T24 (white female patient)	ATCC	HTB-4 TM
Recombinant DNA		
pRP[Exp]-Puro EF1A>hST6GALNAC1 [NM_018414.5] vector	VectorBuilder	VB190819-1167uwn
pRP[Exp]-Puro-EF1A>(Stuffer_300bp) vector	VectorBuilder	VB191025-4255jjz
Software and algorithms		
CXP Software	Beckman Coulter	Version 2.2
Excalibur Qual Browser	ThermoFisher Scientific	V2.2.44
Fiji	on GitHub	GPLv3+
MaxQuant	Max-Planck-Institute of Biochemistry	Version 1.6.17.0
Peak Scanner TM Software	ThermoFisher Scientific	Version 1.0
Phosphomatics	Bio21 Molecular Science and Biotechnology Institute	N/A
Prism software	GraphPad	Version 10
R	R Project for Statistical Computing	Version 4.2.1
Other		
AG 50W-X8 Resin	Bio-Rad	1431441
BioCoat TM Matrigel [®] 24 well plates	Corning [®]	CLS354480
Corning [®] Matrigel [®] Matrix	Corning [®]	356237
Cycloscope TM	Cytognos	CYT-CS-R-50
Mini-PROTEAN TGX Stain-Free Precast Gels 4-20%, 10 well comb, 50ul/well	Bio-Rad	456-8094
MultiScreen-IP Filter Plate, 0.45 μm, clear, sterile	Millipore	MAIPS4510

EXPERIMENTAL MODELS AND STUDY PARTICIPANT DETAILS

Human BLCA cell lines RT4 (white male patient, HTB-2TM), 5637 (white male patient, HTB-9TM), T24 (white female patient, HTB-4TM), and HT1197 (white male patient, CRL-1473TM) were purchased from American Type Culture Collection (ATCC). RT4, 5637, and T24 cells were maintained with complete RPMI 1640 GlutaMAXTM medium (Gibco) and HT1197 with DMEM GlutaMAXTM medium (Gibco) supplemented with 10% FBS (Gibco, 10500-064). Cells were routinely checked for mycoplasma contamination by PCR.⁷⁴ Cell lines were authenticated by the Genomics Scientific Platform at i3s (University of Porto) using the Maxwell 16 System with Maxwell[®] RSC DNA FFPE Kit (Promega Corporation) for genomic DNA extraction and PowerPlex 16 HS System (Promega Corporation) for STR amplification. Detection of the amplified fragments was made with automated capillary electrophoresis using 3500 Genetic Analyzer (Applied Biosystems) and the assignment of genotypes was performed in GeneMapper software v5.0 (Applied Biosystems). Cellosaurus STR similarity search tool was used to compare obtained STR profiles with those available in the Cellosaurus cell line knowledge resource (<https://web.expasy.org/cellosaurus-str-search/>). Cells were kept at 37°C in a 5% CO₂ humidified atmosphere (Normoxia). Cells were also grown for 24h under hypoxia and nutrient deprivation (Hypoxia -Glc) at 37°C in a 5% CO₂, 99.9% N₂ and 0.1% O₂ atmosphere, using a BINDER C-150 incubator (BINDER GmbH), and complete RPMI 1640 or DMEM media without glucose (Gibco). A 24h exposure to 500 μM deferoxamine mesylate salt (DFX, Sigma-Aldrich, D9533) in complete medium was used as a positive control for HIF-1α stabilisation. For re-oxygenation experiments, cells under oxygen and glucose deprivation were restored to standard culture conditions 24 h prior to analysis.

Chicken embryos

The chicken embryo chorioallantoic membrane (CAM) assay was used to assess the *in vivo* establishment of tumour aggregates derived from glycoengineered cell models. On embryonic development day (EDD) 3, a squared window was opened in the eggshell of fertilised chicken (*gallus gallus*) eggs, and 2–2.5 mL of albumen was removed to allow detachment of the developing CAM. The window was then sealed with adhesive tape and the eggs were incubated horizontally at 37.8°C in a humidified atmosphere. On EDD9, 1x10⁶ cells derived from each developed cell model were re-suspended in 10μl of Corning[®] Matrigel[®] Matrix (Corning, 356237) and placed in a 3 mm silicone ring attached to the growing CAM. Control cells and respective glycoengineered models were inoculated in the same egg. At least 10 viable embryos were used per experimental pair. The eggs were re-sealed and returned

to the incubator for one week. On EDD16, the CAM was excised from the embryos, photographed *ex-ovo* under a stereoscope at 20x magnification (Olympus, SZX16 coupled with a DP71 camera), and images were analysed to determine tumour size. CAM attached tumours were then formalin fixed and paraffin embedded and stained with haematoxylin and eosin.

Glycoengineered cell models

A recombinant *Streptococcus pyogenes* Cas9 (GeneArt™ Platinum Cas9 Nuclease, Thermo Fisher Scientific, B25640) and single-guided RNA (GTAAAGCAGGGCTACATGAG, sgRNA, Synthego) were used to generate site-specific double-strand breaks in the *C1GALT1* gene in T24 cells *in vitro*. In parallel, two sgRNAs were used for *GCNT1* gene knock-out (KO) (gRNA1: TAGTCGTCAGGTGCCACCG, gRNA2: AAGCGGTATGAGGTCGTTAA, Stnthego). Lipofectamine™ CRISPRMAX™ Transfection Reagent (Thermo Fisher Scientific, CMAX00001) was used according to the manufacturer's instructions. Complexes were made in serum-free media (Opti-MEM™ I Reduced Serum Medium, Gibco, 31985-047) and added directly to cells in culture medium. Single clones were obtained by serial dilution in 96-well plates and KO clones were identified by Indel Detection by Amplicon Analysis (IDAA) using ABI PRISM™ 3010 Genetic Analyzer (Thermo Fisher Scientific) and Sanger sequencing. Three clones with distinct out of frame indel formation were selected. Single clones with silent mutations provided phenotypic control cell lines. IDAA results were analysed using Peak Scanner Software V1.0 (Thermo Fisher Scientific). Human ST6GALNAC1 (hST6GALNAC1 [NM_018414.5], VectorBuilder) knock-in (KI) was performed in *C1GALT1* KO cells and human ST3GAL1 (hST3Gal1 [NM_173344.3], Vectorbuilder, VB190819-1167uwn) KI was performed in wild-type and *GCNT1* KO cells by conventional mammalian gene expression vector transfection, using jetPRIME® transfection reagent (PolyPlus Transfection, 114-01), according to manufacturer's instructions. Positively transfected cells were selected based on puromycin (2 µg/mL, EMD Millipore, 540222) resistance. In parallel, a mock system containing a 300 bp stuffer ORF (VectorBuilder, VB191025-4255jjz) was established.

Patient samples and ethics

A retrospective series of 70 formalin-fixed paraffin-embedded bladder tumours (FFPE; 30 NMIBC; 40 MIBC) from the IPO-Porto biobank was used for this study after patient's informed consent (ethics project reference: CES 86/017). The mean age of patients was 67 ± 7 years old, with 94% of cases belonging to male patients and 6% female.

METHOD DETAILS

HIF-1α expression

HIF-1α was evaluated using a HIF-1 Alpha ELISA Kit (Invitrogen™).⁷⁵ Procedure steps were followed according to the manufacturer's instructions and results were monitored at 450 nm using a microplate reader (iMARK™, Bio-Rad). The results were normalized to cell proliferation rates.

Proliferation assay

Cell proliferation was determined using a colorimetric Cell Proliferation ELISA (Roche) kit.⁷⁶ Procedure steps were followed according to the manufacturer's instructions and results were monitored at 450 nm using a microplate reader (iMARK™, Bio-Rad).

Lactate assay

A colorimetric Assay Kit (Abcam) was used to detect L(+)-Lactate in deproteinized cultured cell lysates and conditioned medium.⁷⁷ Procedure steps were followed according to the manufacturer's instructions and results were monitored at 450 nm using a microplate reader (iMARK™, Bio-Rad). The results were normalised to cell proliferation rates.

Invasion assay

Invasion assays were performed using BioCoat™ Matrigel® Invasion Chambers with 8.0 µm PET Membrane (Corning®, 356237), according with the manufacturer instructions. Briefly, prior to each experiment, filters were rehydrated in serum-free RPMI 1640 GlutaMAX™ medium (Gibco) medium for 2 h at 37°C. Subconfluent cells were detached using 0.05% Trypsin-EDTA (Gibco, 25300-062,) suspended in culture medium supplemented with 10% inactivated FBS (Gibco, 10500-064), counted, and seeded on the upper side of Matrigel-coated filters at a density of 5 × 10⁴ cells/well. After 24 h of incubation at 37°C, filters were fixed in 4% paraformaldehyde (Sigma-Aldrich, 158127). Non-invading cells on the upper filter surface were completely removed to facilitate analysis. Cells that invaded through the filter were mounted in Vectashield with 4',6-diamidino-2-phenylindole (DAPI, Vector Laboratories, H-1200) and visualized using a Zeiss Axiovert 200M fluorescence microscope.

Invasive cells were quantified by scoring DAPI-counterstained nuclei that passed through the filter pores across at least 12 microscopic fields using a 20x objective. Invasion counts were normalized to cell proliferation rates, and cells were seeded in quintuplicates for each experiment.

Anchorage-independent growth

Anchorage-independent growth was measured using the soft agar colony formation assay.⁷⁸ A 0.5% low melting point agarose (Sea-Plaque®, Lonza, 50101) solution in complete medium was used as the bottom layer in 6-well flat bottom plates. A top layer of 0.3%

agarose containing 1×10^4 cells was then plated and covered with culture medium. Cells were maintained in standard growth conditions for one month. Colonies were then fixed with 10% neutral buffered formalin solution (Sigma-Aldrich, HT501128) and stained with 0.01% (w/v) crystal violet (Sigma-Aldrich, 61135). Colonies were photographed using a stereomicroscope (Olympus, SZX16 coupled with a DP71 camera) and automatically counted using the open-source software ImageJ (Fiji package). Only colonies containing more than 50 cells were considered.

Cell viability assay

Cell viability was determined through the Trypan Blue Exclusion Test of Cell Viability⁷⁹ using Trypan Blue Stain (0.4%) (Gibco, 15250-061). For specific apoptosis stage assessment, cells were detached using Accutase enzyme cell detachment medium (Thermo Fisher Scientific, 00-4555-56) and apoptosis was determined using the Cell Apoptosis Kit with FITC annexin V and propidium iodide for flow cytometry (Thermo Fisher Scientific, V13242), according to the manufacturer's instructions. Data analysis was performed through CXP Software in a FC500 Beckman Coulter flow cytometer.

Cell cycle analysis

Cells were harvested by trypsinisation (0.05% Trypsin-EDTA, Gibco, 25300-062) following fixation and labelling with DNA labelling solution (CycloscopeTM, Cytognos, CYT-CS-R-50) for 10 min at RT in obscurity. Data analysis was performed through CXP Software in a FC500 Beckman Coulter flow cytometer.

Cisplatin resistance

BLCA cells were plated into 96-well plates, following a 24h exposure to crescent concentrations of cisplatin (Accord Healthcare). Positive and negative controls of cell death were set, consisting of cell incubation with complete medium with and without 1% TritonTM-X (Sigma-Aldrich, T8787), respectively. After cisplatin incubation, cells were incubated with 1.2mM 3-(4,5-dimethylthiazol-2-yl)-2,5-diphenyltetrazolium bromide (MTT, Thermo Fisher Scientific, M6494) solution. Formazan crystals were solubilized with dimethyl sulfoxide (Sigma-Aldrich, D26650), following absorbance measurement at 540 nm using a microplate reader (iMARKTM, Bio-Rad). The percentage of cell viability was calculated as follows:

$$\text{Cell viability (\%)} = \frac{\text{Absorbance of treated cells}}{\text{Absorbance of negative control}} \times 100$$

Cell viability was normalized to cell proliferative rates.

Transcriptomics

Total RNA was pooled from five biological replicates of T24 and 5637 cells exposed to normoxia or hypoxia plus glucose restriction using the Qiagen RNeasy Plus Mini kit (Qiagen, 74134). RNA samples were quantified using Qubit 2.0 Fluorometer (Thermo Fisher Scientific) and RNA integrity was checked with Agilent TapeStation (Agilent Technologies). RNA sequencing library were prepared using the NEBNext Ultra RNA Library Prep Kit for Illumina following manufacturer's recommendations. Briefly, mRNA was first enriched with Oligo (dT) beads. Enriched mRNAs were fragmented for 15 min at 94°C. First strand and second strand cDNA were subsequently synthesized. cDNA fragments were end-repaired and adenylated at 3' ends, and universal adapters were ligated to cDNA fragments, followed by index addition and library enrichment with limited cycle PCR. The sequencing libraries were validated on the Agilent TapeStation (Agilent Technologies), and quantified using a Qubit 2.0 Fluorometer (Invitrogen) and qPCR (KAPA Biosystems). The sequencing libraries were clustered on one lane of a flow cell, loaded on a Illumina HiSeq 4000 instrument and sequenced using a 2 × 150 Paired End configuration. Image analysis and base calling were conducted using HiSeq Control Software. One mismatch was allowed for index sequence identification. Garbage reads were trimmed from raw data and BAM files were generated. Unique gene hit counts were calculated using feature Counts from the Subread package v.1.5.2. Only unique reads that fell within exon regions were counted. Since a strand specific library preparation was performed, the reads were strand-specifically counted. After extraction of gene hit counts, the gene hit counts table was used for downstream differential expression analysis. A SNP/INDEL analysis was performed using mpileup within the Samtools v.1.3.1 program followed by VarScan v.2.3.9. The parameters for variant calling were minimum frequency of the alternate allele 25%, *p*-value less than 0.05, minimum coverage of 10, minimum read count of 7. A gene fusion analysis was performed using STAR Fusion v.1.1.0.⁸⁰ Differentially expressed genes between hypoxia and normoxia conditions were assessed using the R-package "DESeq2", and the *p*-values adjusted using False Discovery Rate (FDR) correction. DEGs with a minimum 1-fold change ($|\log_2 \text{ 2-fold change}| > 1$) and with an FDR-adjusted *p*-value lower than 0.05 were selected for downstream analysis. Altered pathways in hypoxia were evaluated using the R-package "gprofiler", with the use of four datasets: gene ontology (GO), Kyoto Encyclopedia of Genes and Genomes (KEGG), WorldPress (WP), and Reactome. Pathways with an FDR-adjusted *p*-value < 0.05 were considered statistically significant.

Metabolomics

Cells were dispersed in 80% methanol (Merck, 34860-1L-R), sonicated for 30 min at 4°C and kept at -20°C for 1 h. Samples were then centrifuged, and the supernatant was analysed by UHPLC-ESI-MS/MS in positive and negative mode. Metabolite analysis was performed using an Ultimate 3000 LC combined with QExactive mass spectrometer (Thermo Fisher Scientific). Eluent A was 0.1% formic

acid (Merk, 5.33002.0050) in water and eluent B was acetonitrile (Merk, 14261-2L). Metabolite separation occurred using the following gradient elution (0-1.5 min, 95-70% A; 1.5-9.5 min, 70-5% A; 9.5-14.5 min, 5% A; 14.5-14.6 min, 5-95% A; 14.6-18.0 min, 95% A). The flow rate of the mobile phase was 0.3 mL/min. The column (Acquity UPLC HSS T3; 100 Å, 1.8 µm, 2.1 mm × 150 mm) temperature was maintained at 40°C, and the sample manager temperature was set at 4°C. Metabolites were identified by retention time and corresponding MS/MS spectra. For metabolomics data pre-processing and analysis, raw data matrices were blank subtracted (a mean blank value was calculated per metabolite) and normalised to the number of cells for each condition. The resulting matrices were then imported to Metaboanalyst 4.0 and log-transformed to reduce heteroscedasticity and Pareto-scaled to adjust for differences in fold changes between metabolites.

Metabolome and metabolome/transcriptome joint pathway analysis

Multivariate and univariate analyses were performed to identify metabolites that discriminate normoxia from hypoxia with low glucose. Unsupervised principal components analysis (PCA) was applied to unravel data structure, following a supervised method, namely partial-least-squares discriminant analysis (PLS-DA) to identify which metabolites were useful to predict group membership. Metabolites with discriminative power were ranked based on Variable Importance in Projection values >1 and PLS-DA models were validated based on the “prediction accuracy during training” test statistic with 1000 permutations ($p < 0.05$ for significance). Heat maps with hierarchical clustering of metabolites were constructed based on: i) distance measure: Pearson correlation (similarity of expression profiles), ii) clustering algorithm: complete linkage (forms compact clusters), iii) feature auto scale. Hierarchical clustering of samples was carried out based on: i) distance measured: Euclidean distance (sensitive to magnitude differences), ii) clustering algorithm: Ward (minimises within-cluster variance). Differences in metabolites between groups were further evaluated using a one-way analysis of variance (ANOVA) with a False Discovery Rate (FDR) cut-off set at 0.05 for significance. Tukey’s post hoc was applied to check which groups differed. Significant metabolites unravelled by ANOVA were then used for pathway analysis to identify the most relevant pathways that are involved in the adaptation of cells from normoxia to hypoxia with low glucose. Pathway analysis was carried out based on: i) functional enrichment, which was assessed using a hypergeometric test for over-representation analysis ($p < 0.05$ for significance) and ii) pathway topology analysis, which was implemented using the relative betweenness centrality. Pathway impact was considered relevant if > 0.1 . The joint pathway analysis was carried out using transcriptomic and metabolomic data, based on a gene and metabolite list with associated fold changes. The human pathway library was chosen using the pathway database “all pathways (integrated)”. The enrichment analysis was based on the hypergeometric statistic test, while degree centrality was used as a topology measure. The integration method was based on a combination of queries.

ATP quantification assay

A fluorometric ATP assay kit (Abcam, ab83355) was used according to the manufacturer’s instructions to determine ATP levels in deproteinized whole-cell lysates. Fluorometric products were quantified at Ex/Em 535/587 nm using a microplate reader (iMARK™, Bio-Rad). The results were normalised to cell proliferation.

Western blot

Whole protein extracts were collected from BLCA cells using a 25 mM Tris-HCl pH 7.2 (Sigma-Aldrich, T6066 & H1758), 150 mM NaCl (Sigma-Aldrich, 7647-14-5), 5 mM MgCl₂ (Sigma-Aldrich, M8266), 1% NONIDET™ (Sigma-Aldrich, 74385), and 5% glycerol (Sigma-Aldrich, G5516) lysis buffer, supplemented with Halt™ Protease and Phosphatase Inhibitor Cocktail (Thermo Fisher Scientific, 78440). Isolated proteins were run on 4–20% precast SDS-PAGE gels (Bio-Rad, 456-8094), and screened for AMPK (Abcam, ab80039), phosphorylated AMPK (Abcam, ab23875), and a panel of glycosyltransferases [C1GalT1 (Novus Biologicals, NBP1-88477), Cosmc (Sigma-Aldrich, HPA015632), B3GnT6 (Invitrogen, PA5-90159), C2GnT (Abcam, ab102665), ST3Gal-I (Abcam, ab96129)]. The antibodies and experimental conditions are detailed in Table S14. The total protein stain was assessed using Ponceau S anionic dye (Sigma-Aldrich, P3504).

Citrate synthase assay

Citrate synthase activity was measured in whole cell protein lysates using the method proposed by Coore et al.⁸¹ In brief, the coenzyme A released from the reaction of acetyl-CoA (Sigma-Aldrich, A2056) with oxaloacetate (Sigma-Aldrich, 328-42-7) was determined by its reaction with 5,5'-dithiobis-(2-nitrobenzoic acid) (Sigma-Aldrich, 69-78-3) at 412 nm ($\epsilon = 13.6 \text{ mM}^{-1} \text{ cm}^{-1}$), using a microplate reader (iMARK™, Bio-Rad). The results were normalized to cell proliferation.

Autophagy assay

Cells were cultured in 96 well plates and submitted to microenvironmental challenges of hypoxia and glucose deprivation. Non-challenged cells were used as control. The presence of autophagy was determined based on the detection of a proprietary fluorescent autophagosome marker using an Autophagy Assay Kit (Sigma-Aldrich, MAK138) according to the manufacturer’s instructions. The fluorescence intensity was measured using a fluorescence microscope (Leica DMI6000 FFW).

Transmission electron microscopy

For electron microscopy, T24 and 5637 cells were fixed in 2.5% glutaraldehyde with 2.5% formaldehyde in 0.1 M sodium cacodylate buffer (pH 7.4) (Electron Microscopy Sciences, 15949). Cells were post-fixed in 1% osmium tetroxide (Electron Microscopy Sciences, 20816-12-0) diluted in 0.1 M sodium cacodylate buffer. Samples were then dehydrated and embedded in Epon resin (TAAB, T031). Ultra-thin 50 nm sections were cut on an RMC Ultramicrotome (PowerTome) using Diatome diamond knives, mounted on 200-mesh copper grids (Electron Microscopy Sciences), and stained with uranyl acetate substitute (Electron Microscopy Sciences, 22405) and lead citrate (Electron Microscopy Sciences, 22410). Sections were then examined under a JEOL JEM 1400 transmission electron microscope (JEOL), and images were digitally recorded using a CCD digital camera Orius 1100W.

Phosphoproteomics and data analysis

The preparation of samples for phosphoproteomics was performed according to Veth, T. S. et al.⁸² Then, samples were suspended in 2% formic acid (Merk, 5.33002.0050) and analysed on an Exploris (Thermo Scientific) coupled to an UltiMate 3000 (Thermo Scientific), fitted with a μ -precolumn (C18 PepMap100, 5 μ m, 100 Å, 5 mm \times 300 μ m; Thermo Scientific), and an analytical column (120 EC-C18, 2.7 μ m, 50 cm \times 75 μ m; Agilent Poroshell). Peptides were loaded in 9% Buffer A (0.1% FA) for 1 min and separated using 9–36% buffer B (80%ACN, 0.1%FA) in 97 min at 300 nL/min, followed by a 6 min column wash with 99% buffer B at 300 nL/min, and a 10-minute column equilibration at 9% B. The MS was operated in DDA mode, with the MS1 scans in a range of 375–1600 *m/z* acquired at 60k, using an automatically set AGC target. MS2 scans were acquired with a 16s dynamic exclusion at a 30k resolution, 28% normalised collision energy, and an isolation window of 1.4 *m/z*. Raw files were processed via MaxQuant version 1.6.17.0 using the verified human proteome from UniprotKB (release 09-2019) containing 20,369 proteins.⁸³ A maximum of 5 modifications and two missed cleavages were set, using fixed carbamidomethyl modification, and the variable modifications oxidised methionine, protein *N*-terminal acetylation, and serine/threonine/tyrosine phosphorylation. The protein and peptide FDR were set to <0.01 and conducted with match between runs enabled. Using the Perseus framework, only class 1 phosphosites were included (>0.75), and with minimally two detections in at least one group for subsequent analysis. Missing values were replaced using the normal distribution and a downshift of 1.8. The data was subsequently explored using Phosphomatics.⁸⁴

Glycomics

The *O*-glycome of BLCA cells challenged by microenvironmental stressors as well as glycoengineered cell models was characterized through the Cellular *O*-glycome Reporter/Amplification method,⁸⁵ using the protocol detailed in Fernandes, E. et al.⁸⁶ The *O*-glycome of oesophageal, gastric, and colorectal cancer cells as well as human monocyte-derived macrophages was also characterised following the same protocol. Regarding bladder tumours, *N*- and *O*-glycomics were performed as previously described.⁸⁷ Briefly, FFPE tissues were deparaffinized, rehydrated, and subjected to heat-induced antigen retrieval using a citrate-based solution (Vector Laboratories, H-3300-250). Then, proteins were denatured and reduced by incubation with 150 μ l denaturation mix [145 μ l of 8 M GuHCl (Sigma-Aldrich, G4505) and 5 μ l of 200 mM DTT (Sigma-Aldrich, D9779) at 60°C for 30 min. *N*-glycan release was achieved after digestion with PNGase F (1 U/10 μ g protein at 37°C overnight; Promega, PROMV4831). Released *N*-glycans were hydrolysed with 25 μ l of 100 mM ammonium acetate (Sigma-Aldrich, A7330) at pH 5 (1 h at RT), removing the glycosylamine form of the non-reducing terminus, and subsequently reduced with 20 μ l of 1 M NaBH₄ (Honeywell Fluka™, 71321) in 50 mM KOH [3 h at 50°C, Sigma-Aldrich, 306568]. The reaction was quenched by adding glacial acetic acid (Sigma-Aldrich, A6283). *O*-glycans were released by reductive β -elimination (1 M NaBH₄ in 50 mM KOH overnight at 50°C). Finally, reduced *N*- and *O*-glycan samples were desalted using a cation exchange resin (Bio-Rad, AG 50W-X8). *N*-glycomics of BLCA cell lines was performed similarly after immobilisation of membrane protein extracts in a hydrophobic PVDF membrane (Millipore, MAIPS4510). All glycans were permethylated and analysed by reverse phase nanoLC-ESI-MS/MS as previously described by us,⁸⁶ using a 3000 Ultimate nano-LC coupled to either an LTQ-Orbitrap XL or QExactive mass spectrometer (Thermo Fisher Scientific). Glycan structures were identified considering previous knowledge of glycosylation, chromatography retention times, *m/z* identification, and corresponding product ion spectra. The relative abundance resulted from the sum of the extracted ion chromatogram areas for each glycan structure (singly, doubly, and/or triply charged ions) in relation to the sum of chromatographic areas of all identified glycans using Excalibur Qual Browser V2.2.44 (ThermoFisher Scientific).

Flow cytometry for glycans detection

BLCA cells were screened for Tn, STn, T, and ST antigens as well as for *N*-acetylglucosamine residues by flow cytometry. Briefly, adherent cells were detached using the non-enzymatic cell dissociation reagent Versene (Gibco, LTI 15040-066) and fixed in 2% paraformaldehyde (Sigma-Aldrich, 158127),⁸⁰ following lectin staining. Lectins and experimental conditions are detailed in Table S14. Comparison of Tn and STn expressions was performed using VVA lectin before and after Neuraminidase (Sigma-Aldrich, N5631) treatment, after ensuring complete desialylation. Neuraminidase treatments have been optimised to ensure full desialylation, as confirmed by MS analysis. Regarding GSL II lectin detection, PNGaseF enzymatic digestion was performed to exclude *N*-glycan-associated *N*-acetylglucosamine residues contribution. Data analysis was performed through CXP Software in a FC500 Beckman Coulter flow cytometer.

Immunocytochemistry and immunohistochemistry

Immunofluorescence (IF) was performed to evaluate Tn, STn, T and sialyl-T antigens in T24 glycoengineered cell models using the same lectins and strategies employed in flow cytometry. Cells were cultured at low density and fixed with 4% paraformaldehyde (Sigma-Aldrich, 158127). After antigen staining (Table S14), cells were marked with $2,3 \times 10^{-3}$ $\mu\text{g}/\mu\text{L}$ 4',6-Diamidino-2-phenylindole dihydrochloride (DAPI, Thermo Fisher Scientific, 62247) for 10 min at RT in the dark. Sialylated glycoforms were evaluated in parallel with samples digested with 50 mU/mL neuraminidase (Sigma-Aldrich, N5631) overnight at 37°C. Tumours were also screened by immunofluorescence envisaging Tn, ST, and HIF-1 α co-detection. All images were acquired on a Leica DMI6000 FFW microscope using Las X software (Leica). Furthermore, BLCA FFPE tissue sections were screened for Tn, STn, T, ST, SLe^A, SLe^X, HIF-1 α , and KI-67 antigens by immunohistochemistry (IHC) using the streptavidin/biotin peroxidase method. Briefly, 3 μm sections were deparaffinized with xylene (Sigma Aldrich, 33817), rehydrated with graded ethanol (EMD Millipore, 1.00983.2511) series, microwaved for 15 min in boiling antigen unmasking solution (Vector Laboratories, H-3300), and exposed to 3% hydrogen peroxide in methanol for 20 min. Antibodies and experimental conditions used for immunoassays are detailed in Table S14. Antigens were identified with VECTASTAIN® Elite® ABC HRP Reagent (Vector Laboratories, PK-7100) followed by incubation with ImmPACT® DAB Substrate (Vector Laboratories, SK-4105). Finally, the slides were counterstained with haematoxylin for 1 min.

Immuno-reactive sections were blindly assessed using light microscopy by two independent observers and validated by an experienced pathologist.

RT-PCR for glycogenes expression

C1GALT1, *C1GALT1C1*, *B3GNT6*, *GCNT1*, *GCNT2*, *GCNT3*, *GCNT4*, *B3GNT3*, *FUT1*, *FUT2*, *FUT3*, *FUT4*, *FUT5*, *FUT6*, *FUT7*, *FUT9*, *ST3GAL1*, *ST3GAL3*, *ST3GAL4*, *ST6GANAC1*, *ST6GALNAC2*, *ST6GALNAC3*, and *ST6GALNAC4* gene expression was assessed by quantitative polymerase chain reaction. Briefly, total RNA from cultured cells was isolated using TriPure Isolation Reagent (Roche, 11667165001), according to the manufacturer instructions.⁸⁸ RNA conversion and gene expression analysis were performed using TaqMan™ Gene Expression Assays (Applied Biosystems™). The mRNA levels were normalised to the expressions of *B2M* and *HPRT* housekeeping genes.⁸⁹ Taqman probes used for the glycogenes screening are detailed in Table S15.

QUANTIFICATION AND STATISTICAL ANALYSIS

Public gene expression and clinical data statistical analysis

Normalised gene expression data and the corresponding clinical data, including survival information, for 407 bladder cancer patients were obtained from The Cancer Genome Atlas (TCGA) database using the Xena browser. In addition, normalised gene expression data from healthy bladder tissue samples (n=9) from the Genotype-Tissue Expression (GTEx) project was also retrieved. Univariable Cox regression analysis was used to analyse and identify a survival-associated hypoxia gene signature. Hazard ratios (HRs) and corresponding 95% confidence intervals (CIs) were estimated for the 30 most differentially expressed genes in hypoxia and low glucose conditions using the “finalfit” R package. Kaplan-Meier (KM) analysis and log-rank test were performed to evaluate the survival outcomes in the patients with the hypoxia gene signature identified. The optimal cutoffs to categorise the expression of each gene in “high” or “low” were determined by the “surv_cutpoint” algorithm of the “survival” R package. Heatmaps were constructed using the “ComplexHeatmap” R package, to assess gene expression profile between conditions, hypoxia versus normoxia. *p*-value <0.05 was considered statistically significant. All statistical analyses were performed using R (version 4.2.1).

Statistical analysis

Statistical analyses were performed using the GraphPad Prism software. One-way ANOVA followed by Tukey's multiple comparisons test was used in evaluation of HIF-1 α , lactate, proliferation, invasion, and the autophagy experiment. The Mann-Whitney test was used in the analysis of cisplatin IC50, L-carnitine and citrate levels, glycosyltransferases expression, AMP/ATP ratio, glycans expression data from flow cytometry assay, and relative abundance of O- and N-glycans extension in tumours. The Mann-Whitney test was also used in the evaluation of AMPK expression and the Two-way ANOVA followed by Tukey's multiple comparisons test was used for glycoengineered cells' proliferation and invasion. Finally, an unpaired t-test was used in the analysis of the percentage of HIF-1 α -positive tumour area and for colony-forming assays. CAM assay results were analysed using a Wilcoxon test. Statistical analysis of phosphoproteomics data was performed in Phosphomatics software.⁸⁴ Differences were considered significant for *p*<0.05. All experiments were performed in triplicates and three replicates were conducted for each independent experiment. The results are presented as the average and standard deviation of these independent assays. The statistical details of experiments can also be found in the figure legends.